Inverse magnetic catalysis in QCD and holography

Govert Nijs 3477223

Supervisors:
Umut Gürsoy Yuri Kuznetsov

June 30, 2016

Abstract

A holographic model of a QCD-like theory in a magnetic background is studied in the limit of an infinite number of colors N_c and infinite massless quark flavors N_f, where the ratio $x = N_f/N_c$ is kept constant at 1. The gravitational model contains two scalar bulk fields, namely a dilaton λ, which is the source of $\mathrm{tr}\, F^2$, with F the gluon field tensor, and a tachyon sourcing the chiral condensate $\langle \bar{q}q \rangle$. This model is used to compute both the chiral and the deconfinement phase transition temperatures, as well as the chiral condensate. This leads to a computation of the phase diagram of QCD in the (T, B)-plane, as well as the observation of inverse magnetic catalysis of the chiral condensate by the magnetic field, in qualitative agreement with lattice results.

Contents

1 Introduction

Quantum Chromodynamics (QCD) is the theory describing the strong interactions. Developed in the mid-twentieth century, it describes hadrons in terms of smaller constituent particles called quarks and gluons. Mathematically, it is a Yang-Mills (YM) theory based on the Lie group $SU(3)$, where 3 is the number of colors of the theory. Its predictions made using perturbative QCD have all been verified in particle accelerator experiments. However, in recent years, it has been confirmed at RHIC in Brookhaven and at the LHC in Geneva, that there are also strong phenomena which cannot be described in the weak coupling limit. Next to the known hadronic bound states, it turns out that the theory includes a new state of matter, in which quarks are not bound together in sets of two or three, but instead propagate freely. This deconfined state is called a Quark Gluon Plasma (QGP), and it is well-described using hydrodynamics, which indicates that strong coupling effects are important.

An interesting problem is what happens if a magnetic field[1] is applied to QCD matter. This has a few interesting consequences. Firstly, the Landau levels will shift, causing the masses of the excitations of the vacuum to change. Another is the appearance of anomalous transport phenomena and quantum anomalies, such as the generation of an electric current as a consequence of the magnetic field, called the Chiral Magnetic Effect. Effects indicating this, as well as a related phenomenon called the Chiral Vortical Effect, have been seen in heavy ion experiments[1]. Also, the CME has also been observed in condensed matter systems[33]. Another thing one can look at is the phase diagram of QCD in the (T, B)-plane, looking in particular at the effects of the magnetic field on the phase transition temperature between the confined and the deconfined phases. Lastly, the effect on chiral symmetry breaking can be studied. The order parameter describing this transition, called the chiral condensate, can either increase with increasing B, or it can decrease. In the first case we call it magnetic catalysis, in the latter inverse magnetic catalysis.

The latter two, namely the phase diagram and the (inverse) magnetic catalysis, is what this thesis will focus on. In the weak coupling limit, it is possible to show that magnetic catalysis occurs[35]. At strong coupling, it is not possible to do perturbative calculations. In this situation, there are two ways to proceed, of

[1]Here, and in the entire thesis, this will denote an electromagnetic magnetic field, not a gluonic magnetic field.

which the first is to do lattice QCD computations. In this method, space-time is assumed to be discrete, allowing a Monte Carlo approximation of the Euclidean path integral. It has been used successfully to compute both (inverse) magnetic catalysis effects and the temperature dependence of the deconfinement temperature. Although these computations are still not confirmed by experiments, they are generally regarded as reliable, since they make no additional assumptions other than the QCD Lagrangian. The other method, the one we will be using, is to use the holographic principle to try to come up with a dual gravitational theory in which the results can be computed more readily.

The above leads to the following problem statement: Can we, using holographic methods, find out what happens in QCD at strong coupling, and particularly, what the dependence on a background magnetic field is? Is it possible to understand the lattice results in a holographic setting? If so, then this would be a step forward, since this would mean a step closer to an analytic understanding of these phenomena.[2] For vanishing B, several holographic results are already known[2], and in recent weeks there has also been a publication, using a different model from the one in this thesis, for non-zero B[20].

These questions are not just academic ones, but they also possibly influence experimental results. Strong magnetic fields of the order of 10^{19} Gauss can be found at the center of heavy ion collision experiments. In these experiments, heavy atoms such as gold (RHIC, Brookhaven, NY) or lead (LHC, Geneva) are stripped of their electrons, and collided at energies high enough to create a QGP. Most of these collisions are off central collisions such as the one shown in figure 1. The parts which do not participate directly in the collision process are highly charged, and they move at almost the speed of light, so the magnetic fields generated are indeed enormous. These large fields only exist in a very small region for a very short amount of time, but its location and time of existence overlap with the location and moment in which the QGP exists. Understanding the QGP in this setting will require an understanding of the influence of these magnetic fields on the QCD dynamics. Since the QGP is governed by strong interactions, it requires non-perturbative methods to address these questions, such as lattice QCD and the AdS/CFT correspondence.

As mentioned before, we will study this problem by using holography, or the AdS/CFT correspondence. The holographic principle was inspired by the early results of Hawking and Bekenstein that black holes have a temperature and an entropy, the latter of which is proportional to its area[28, 8]. It was then proposed by 't Hooft[39] and Susskind[37] that the description of a region of space can be encoded on the boundary of such a space. A more rigorous theory relating a 4D super Yang-Mills theory to a gravitational model in 5D was subsequently proposed by Maldacena[34]. Today, the correspondence is developed enough so that we can use it to relate a QCD-like theory to a gravitational model in 5 dimensions. Note that this QCD-like theory will not be exactly QCD, but it is believed that the resemblance is good enough so that results will be applicable to QCD.

The rest of this thesis has the following structure: First prior results on (inverse) magnetic catalysis will be discussed in more detail, then the AdS/CFT correspondence will be discussed in detail, as well as an improvement over classic

[2]The methods used are mostly analytic, only the equations of motion are solved numerically.

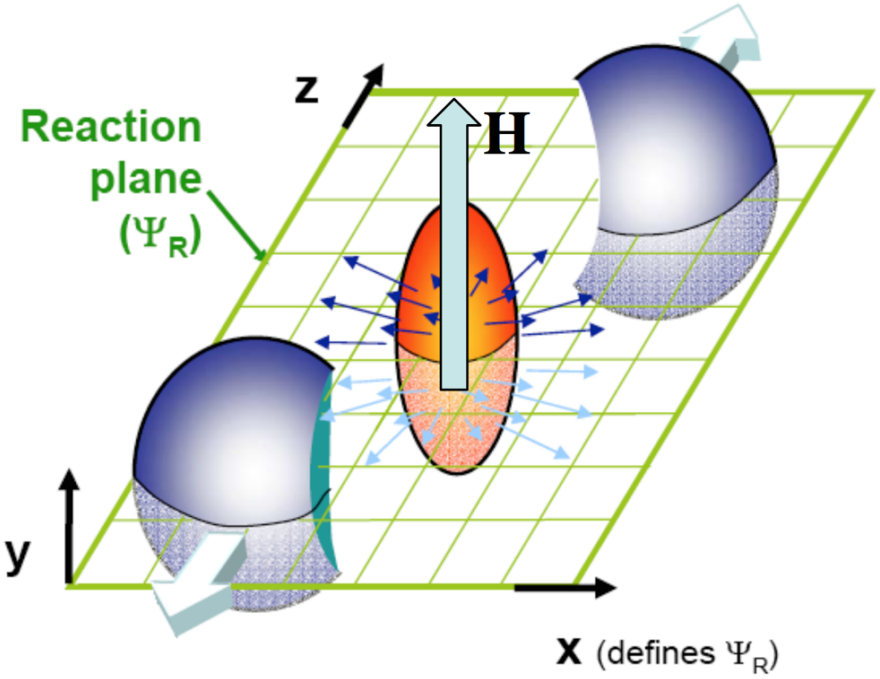

Figure 1: Schematic of an off central heavy ion collision. It can be seen that the overlapping parts of the ions interact to form a QGP, while the other parts continue moving. Being charged with many elementary charges and moving at very high speeds, these result in large magnetic fields of the order of 10^{19} Gauss. This image was taken from [32].

AdS/CFT that we will be using, called Improved Holographic QCD (IHQCD). Next, the gravitational model we use will be introduced. This includes a discussion of the action, the equations of motion and its symmetries, and the on-shell action. The equations of motion will be solved with the appropriate boundary conditions, and the thermodynamics of the model will be extracted from the solutions. This in turn enables us to use the solutions to construct the phase diagram, and to do a computation of the chiral condensate, which enables us to draw conclusions on the problem statement. Finally, an outlook on potential further research will be given. Wherever the computations get very involved, the computations have been moved to an appendix. Care has been taken to make sure the main text is independent of the details discussed in the appendices.

Of these subjects, my personal contributions have been to derive the equations of motion, its symmetries, on-shell action and near-boundary expansion, as well as a modification to the w potential, which is to be introduced along with the action and which causes the observed effect to be more pronounced. In addition to this, other contributions are to apply the techniques from [2] to this new model, and to develop the new method of computing the chiral condensate detailed in appendix B. Last among these contributions are the algorithms for finding the exact phase transitions shown in appendix C. Of these contributions, several are of mathematical interest. These are the large derivations such as that of the equations of motion and the on-shell action, the near-boundary expansion and the numerical techniques used in appendices B and C. Wherever these mathematically interesting parts occur outside of the appendices, they will be emphasized as such.

2 (Inverse) magnetic catalysis

As was mentioned in the introduction, (inverse) magnetic catalysis is one of the two phenomena which will be studied in this thesis. This section will discuss chiral symmetry breaking and why it can be expected that an external magnetic field influences this effect. After this, different methods of computing (inverse) magnetic catalysis will be discussed, and the section will end with a lattice QCD result that this thesis will attempt to match with a different method.

Chiral symmetry breaking is an example of spontaneous symmetry breaking, involving the condensation of quark-antiquark pairs, so that $\langle \bar{q}q \rangle$ attains a non-zero value. This condensate is responsible for the generation of most of the mass present in hadrons. Since magnetic fields tend to align spins, the formation of pairs is expected to be influenced by such an external magnetic field. For a precise computation, several methods are available. Examples are perturbative models and, more recently, lattice models and holography.

Historically, the first of these to be used were perturbative models. Of these, perturbative QCD is of course used, but also effective theories like the Nambu-Jona-Lasinio (NJL) model[27]. In these models, it is found that the presence of a magnetic field increases the chiral condensate, so this means that in these models magnetic catalysis is observed[35]. As an example, in 2 spatial dimensions, at tree level one has the following expression for the chiral condensate.

$$\langle \bar{q}q \rangle = -\lim_{u \to u'} \mathrm{tr}[S(u, u')],$$

with S the fermion propagator, which in Euclidean space has the following

Fourier transform:

$$\tilde{S}_E(k) = -i \int_0^\infty \mathrm{d}s \exp\left[-s\left(m^2 + k_3^2 + \mathbf{k}^2 \frac{\tanh(eBs)}{eBs}\right)\right] \times \left(-k_\mu \gamma_\mu^E + m + i(k_2\gamma_1^E - k_1\gamma_2^E)\tanh(eBs)\right)\left(1 + i\gamma_1^E\gamma_2^E \tanh(eBs)\right).$$

This leads to the following expression for the condensate:

$$\langle \bar{q}q \rangle = -\frac{4m}{(2\pi)^3} \int \mathrm{d}k_3 \, \mathrm{d}^2\mathbf{k} \int_{1/\Lambda^2}^\infty \mathrm{d}s \exp\left[-s\left(m^2 + k_3^2 + \mathbf{k}^2 \frac{\tanh(eBs)}{eBs}\right)\right],$$

with Λ an ultraviolet cutoff, and m the quark mass. Assuming zero quark mass and taking the limit $\Lambda \to \infty$, one then obtains

$$\langle \bar{q}q \rangle = -\frac{|eB|}{2\pi} \operatorname{sign}(m).$$

Note that although the condensate becomes more negative with increasing magnetic field, this still indicates magnetic catalysis, because the absolute value of the condensate still increases.

Analogously, one can obtain a similar result in 3 spatial dimensions:

$$\langle \bar{q}q \rangle = \langle \bar{q}q \rangle_0 \left(1 + \frac{|eB|^2}{3\langle \bar{q}q \rangle_0^2 \log(\Lambda/\sqrt{\langle \bar{q}q \rangle_0})^2}\right),$$

In perturbative QCD, computations analogous to the one above can be done with the same conclusion. Hence there is magnetic catalysis in perturbative QCD. with $\langle \bar{q}q \rangle_0$ the chiral condensate in the absence of a magnetic field. However, these computations all assume weak coupling, and we know that the quark gluon plasma is strongly interacting, which means that perturbative methods are not well-suited to compute these properties.

One solution to this problem is to use lattice QCD. Conceptually, this is a very simple approximation, which assumes space-time to be discrete. Operators in the theory can then be computed by means of the Euclidean path integral, which can be evaluated by means of a Monte Carlo simulation. This method has a clear advantage, namely that it makes no additional assumptions over the QCD action, and that it is non-perturbative. This gives a high degree of credibility to its results in the strong coupling regime. There are also difficulties though, the most major being that this type of simulation is very memory-intensive. This severely limits the lattice sizes used, and to extract useful results multiple lattice sizes have to be computed, and the continuum limit has to be extracted from all of them. Also, in taking this continuum limit, care must be taken to renormalize the theory so that it matches the renormalization used in perturbative QCD computations.

Lattice QCD has indeed been used to compute (inverse) magnetic catalysis[13, 12, 9, 17, 18, 6, 5, 7, 16, 29, 30, 15, 10, 11], and a result is shown in figure 2. In this result, the deconfinement transition temperature is shown. This is the phase transition between the deconfined QGP phase and the confined hadronic phase. Lattice results show that the deconfinement transition and the chiral transition where chiral symmetry are broken coincide.[3] This means that

[3]Note that for massive quarks the transitions become cross-overs, but the approximate locations of the cross-overs coincide approximately.

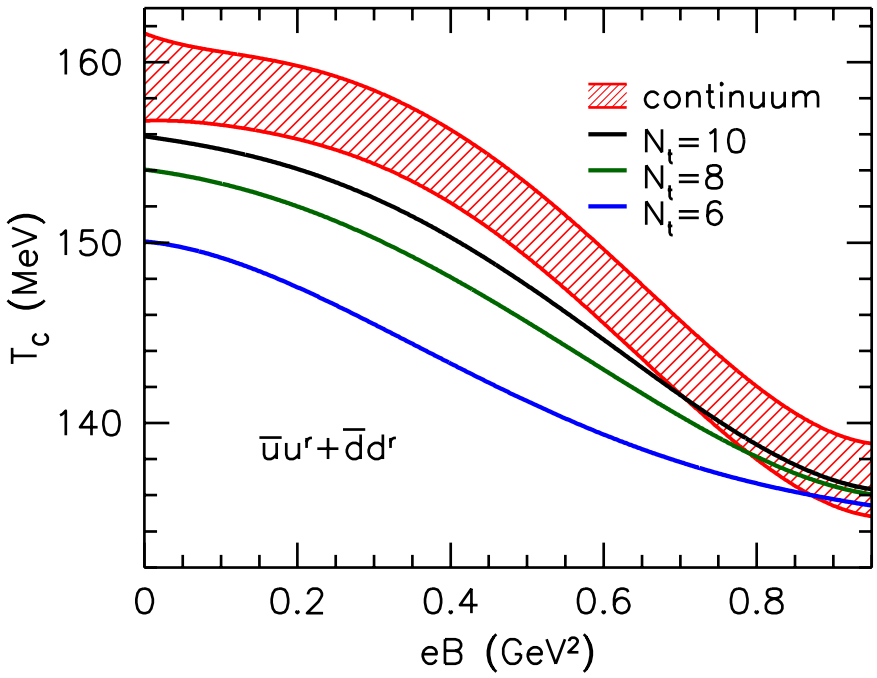

Figure 2: Inverse magnetic catalysis as computed by means of lattice QCD. It can be seen that three different lattice sizes have been used, and that the continuum limit has been estimated. Figure taken from [6].

we can also interpret the result in figure 2 as the chiral transition. In this picture, at temperatures below the transition, chiral symmetry is broken and excitations become massive. Above the transition, chiral symmetry is preserved, and excitations are massless.[4] This means that the lattice result shows inverse magnetic catalysis at finite T, since if we start in the chirally broken phase and increase the magnetic field while keeping the temperature constant, the chiral condensate will decrease and eventually disappear as we cross the chiral transition. Note though that at $T = 0$, lattice QCD also shows magnetic catalysis, in accordance with the perturbative result. Also note that the lattice results depend on the quark masses. Only if these are taken to be small, one observes inverse magnetic catalysis. Otherwise one observes magnetic catalysis[17, 18].

As mentioned in the introduction, we will use holography to try to reproduce this result. In the next section, holography will be introduced.

3 The AdS/CFT correspondence

As was already mentioned in the introduction, AdS/CFT provides a duality between a quantum field theory in 4 dimensions on the one hand, and a gravitational theory with bulk fields in 5 dimensions. In this section, the AdS/CFT correspondence will be motivated by the historical arguments which led to it. Next, the correspondence will be posed, and it will be explained in which limit the gravitational theory simplifies to classical GR. Also, it will be explained how to compute expectation values of operators in the QFT in terms of the bulk fields in the gravitational theory. Some other things which need to be introduced in order to apply the correspondence to a theory resembling QCD at a finite temperature are naturally how to introduce a finite temperature, but also how to see whether the theory at that temperature is confining or not. Lastly it will be discussed how to introduce flavor into the model.

As was mentioned in the introduction, the first hint of the holographic principle was given by the fact that the entropy of black hole is proportional to the area of its event horizon. In order to not have any conflict with the second law of thermodynamics, the entropy of a black hole must be the maximum entropy that that given volume of space-time can have. Since the entropy encodes the amount of information in the system, this means that the information of that region of space-time must be somehow encoded on its boundary. Another, seemingly unrelated, idea is the 't Hooft large N_c approximation[38]. In this approximation, computations in an $SU(N_c)$ gauge theory are performed by expanding the result in powers of $1/N_c$, keeping the coupling constant $\lambda = g^2 N_c$ constant.[5] For QCD, even though N_c is only 3, this seems to work well. The remarkable thing is that the perturbation expansion is now not in the number of loops in the Feynman diagrams, but rather the genus of the surfaces in which the Feynman diagrams can be embedded without any lines crossing. This is very similar to the worldsheet expansion in string theory, and the limit required by it turns out to be the same limit that will be required to simplify the gravitational side of the AdS/CFT correspondence.

[4] This is not entirely true since quarks have a small mass. However, in hadrons most of the mass comes from chiral symmetry breaking, and in the holographic computations in this thesis quarks will therefore be assumed to be exactly massless.

[5] Here g is the Yang-Mills coupling constant.

This makes it come as no surprise that AdS/CFT as formulated by Maldacena[34] and others [40, 21] is derived from string theory. Its ingredients are D-branes in type IIB string theory. D-branes are non-perturbative membrane-shaped excitations of string theory on which open strings end, which in type IIB string theory come in 1, 3, 5 and 7 dimensions. An important observation for the AdS/CFT correspondence is that if we take N_c parallel coinciding Dp-branes, in the low energy limit we find a $U(N_c)$ gauge theory with $9-p$ scalar fields in the adjoint representation of $U(N_c)$[14]. In particular, if we take these branes to be D3-branes, then the low energy theory is precisely $\mathcal{N}=4$ supersymmetric Yang-Mills (SYM) theory with $U(N_c)$ as its gauge group. It turns out that the diagonal $U(1)$ subgroup of $U(N_c)$ decouples from the rest, and can be integrated out. The leftover gauge group is then precisely the required $SU(N_c)$. Also, since the D3-branes have 3 spatial dimensions, in the low-energy limit, the open strings are effectively constrained to these $3+1$ dimensions, so that we're left with a 4-dimensional SYM theory with $SU(N_c)$ as its gauge group. The interesting part is now that because string theory is a theory including gravity, we know that these branes must gravitate. The supergravity equations are exactly solvable, and it turns out that the resulting geometry is that of $\mathrm{AdS}_5 \times S^5$. This means that we have two different descriptions of the D3-branes, and therefore the low-energy limits should match in particular[14]:

$$\{\mathcal{N}=4SU(N_c) \text{ SYM theory}\} = \{\text{type IIB string theory in } \mathrm{AdS}_5 \times S_5\}\,.$$

We will next make this more precise, but first consider figure 3. This is a

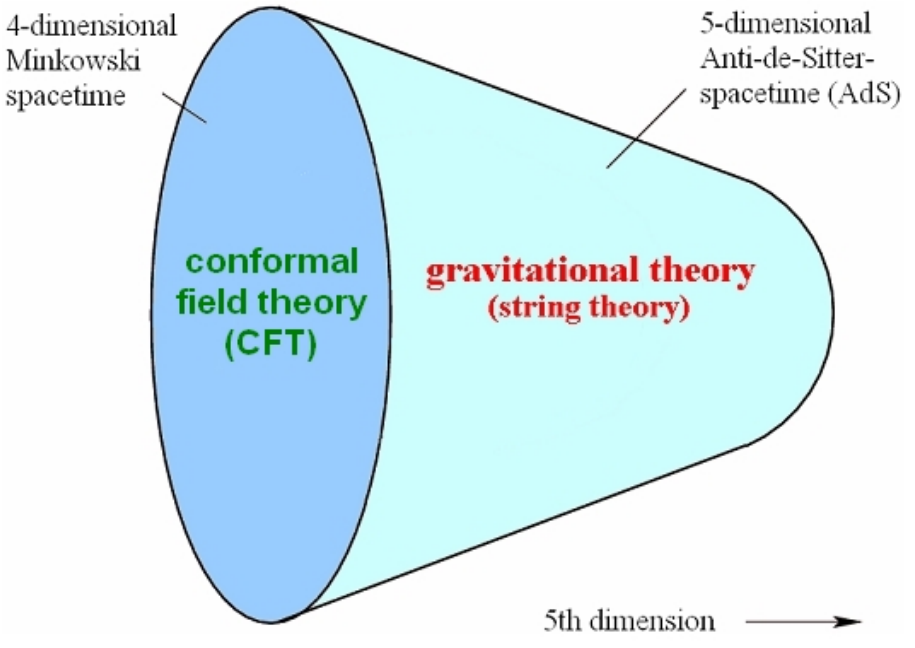

Figure 3: Intuitive picture of the AdS/CFT correspondence. The quantum field theory can be thought of as living on the boundary of the AdS space.

convenient way of thinking about AdS/CFT. The quantum field theory can be

thought of as living on the boundary of the AdS space, where the boundary is defined as the hyperplane where $r = 0$ in the following AdS_5 metric:

$$ds^2 = \frac{R^2}{r^2}\left(\eta_{\mu\nu}\,dx^\mu\,dx^\nu + dr^2\right).$$

where R is the AdS radius. The extra dimension r can in this picture be identified with the energy scale of the theory. In the quantum field theory, there are two important parameters, namely the number of colors N_c and the 't Hooft coupling $\lambda = g^2 N_c$. It turns out that these can be related to the two important parameters in the string theory picture. These are the string length ℓ_s, which determines how important the excitations of the strings are, and the string coupling, which is related to the gravitational constant G and which determines how important string interactions are. We have the following relations[14]:

$$\frac{G}{R^8} \propto \frac{1}{N_c^2}, \qquad \frac{\ell_s^2}{R^2} \propto \frac{1}{\sqrt{\lambda}}.$$

This means that the string theory side reduces to classical GR in the limit where $N_c \to \infty$ and $\lambda \to \infty$. Note that this is quite remarkable; As the interactions in the QFT get larger, the dual theory becomes easier. The price we have to pay for this is that we also have to take $N_c \to \infty$. However, as remarked earlier, for QCD this limit has little effect on the results.

The next thing to discuss is the way in which we can compute expectation values of operators in the quantum field theory in terms of the bulk gravitational theory. This method is called the operator-field correspondence. Say we have an operator $\mathcal{O}(x)$ in the quantum field theory which is sourced by a field $\phi(x)$. Then the gravitational theory will have a field $\Phi(r, x)$ such that near the boundary we have

$$\Phi(r, x) \approx \phi(x) r^{d-\Delta} + \frac{\langle \mathcal{O}(x) \rangle}{2\nu} r^\Delta,$$

with

$$\Delta = \frac{d}{2} + \nu, \qquad \nu = \sqrt{m^2 R^2 + \frac{d^2}{4}},$$

and with m the mass of the bulk field. In words, the bulk field dual to the operator $\mathcal{O}$ has two boundary modes: one non-renormalizable term which contains the source of the operator, and one renormalizable term which contains the vacuum expectation value of the operator in the presence of the source. A few examples of operators and their corresponding bulk fields are given in table 1. These examples are all operators/fields which will appear in the holographic model to be introduced in the next section.

Until now there has been an important ingredient missing, namely a finite temperature. This can be introduced by introducing Euclidean time $t \to -it_E$ and replacing the AdS metric with a metric such as this one:

$$ds^2 = \frac{R^2}{r^2}(f(r)\,dt_E^2 + dx_1^2 + dx_2^2 + dx_3^2) + \frac{R^2}{r^2 f(r)}\,dr^2,$$

with $f(0) = 1$ and $f(r_h) = 0$ for some horizon value $r = r_h$. In other words, it is a metric which is AdS near the AdS boundary at $r = 0$, but it also has a black hole horizon. In this picture, the black hole horizon contains both

QFT operator	Bulk field
$T^{\mu\nu}$	$g_{\mu\nu}$
$\mathrm{tr}\, F^2$	ϕ
$\bar{q}q$	τ

Table 1: Examples of operators and their corresponding fields, which are related through the operator-field correspondence. The stress-energy tensor is dual to the metric, the trace of the gluon field tensor squared is dual to the dilaton field (to be introduced in the next section), and the quark-antiquark correlator, the vacuum expectation value of which is the chiral condensate, is dual to a tachyonic scalar field.

the temperature and the entropy. The temperature is given by the Hawking temperature of the black hole, and the entropy is given by the Bekenstein-Hawking temperature:

$$T = \frac{-1}{4\pi}\frac{\partial f}{\partial r}\bigg|_{r=r_h}, \qquad S = e^{3A}.$$

Another quantity for which the gravitational dual becomes clear in this picture is the Helmholtz free energy. As the partition functions of the quantum field theory and its gravitational dual are equal by the correspondence, it makes sense that the on-shell actions of the Euclidean action are also equal. This leads to the identification of the free energy of the quantum field theory with the on-shell action of the Euclidean gravitational action. Another property of QCD, namely confinement, is closely related to that of introducing finite temperature. It turns out that black hole solutions are deconfined, while those without a black hole are confined. In this way, the confined solutions correspond to the zero-temperature solutions. These confined solutions are also denoted as thermal gas solutions.

The discussion in the previous paragraph immediately leads to one of the phase transitions that will be considered in this thesis, namely the deconfinement transition. Confined solutions, although they correspond to the zero-temperature solutions since they don't have a black hole, exist for any temperature, and, as it turns out later, also for any magnetic field B. This means that for each (T, B)-pair we will be able to look whether the system is confined or not. If a black hole solution for that pair exists and its free energy is lower than that of a thermal gas solution, then the system will be deconfined. Else it is confined. Obviously the boundary between these two situations corresponds to the deconfinement transition temperature $T_c(B)$.

Another ingredient that we will need in this thesis is flavor. Until now all fields have transformed under the adjoint representation of the gauge group, while quarks in QCD are known to transform under the fundamental representation. It turns out that flavor can be introduced by introducing N_f D-brane probes, where N_f is the number of flavors. In QCD in the regime we're looking at, the number of flavors is 3, since the heavier c, b and t quarks are too heavy to participate. Taking N_f to be some fixed value, in the holographic picture we arrive at $N_f \ll N_c$, which is called the 't Hooft limit. In fact, in the holographic picture, it is not straightforward what N_f should be. Since N_c is also 3 in QCD, we have two options. The first is the 't Hooft limit as discussed above, while the second keeps not N_f, but $x \equiv N_f/N_c$, constant. This is called the Veneziano

limit. In this thesis, we will take this limit, and we will also set $x = 1$, which keeps the ratio between N_f and N_c fixed at what it is in ordinary QCD. However, there is no rigorous argument why this is the correct number, and indeed many other possibilities have been explored[3].

This ingredient leads to the other phase transition, called the chiral transition. As was already seen before in table 1, the vacuum expectation value $\langle \bar{q}q \rangle$ is called the chiral condensate. It is the order parameter of chiral symmetry breaking. Of the black hole solutions, some solutions will have $\langle \bar{q}q \rangle = 0$, corresponding to chiral symmetry being preserved, and others will have $\langle \bar{q}q \rangle \neq 0$, corresponding to chirally broken solutions. As before, if multiple such solutions exists, one should check which has the lowest free energy. This solution will be the dominant phase. Also as before, the boundary between where chirally symmetric solutions dominate and where chirally broken solutions dominate corresponds to the chiral transition temperature $T_\chi(B)$.

Finally, there is the issue of constructing the gravitational action. There are two approaches for this. It is possible to start from string theory and construct the theory there. Subsequently one would derive both the corresponding QFT and the corresponding bulk theory. This has one major disadvantage though, namely that it is very difficult to arrive at a QFT resembling QCD this way. Luckily, there is another way, which is the method we will be using. In this approach, we start from the gravitational theory right away, and construct a general action. Such an action will contain several potential functions, the shapes of which influence properties of the quantum field theory. By matching these to known properties of QCD, we can constrain the potential functions to arrive at a good gravitational analog for QCD. In this thesis, the starting point has been the potential functions as defined in [2], which are known to give a good analog for QCD at zero magnetic field and even also in the presence of a quark chemical potential.

3.1 Improved Holographic QCD

The previous discussion has been a general discussion on the AdS/CFT correspondence. In this section, we'll discuss a particular class of holographic models called Improved Holographic QCD (IHQCD), of which the model we use is a particular example. The defining feature of IHQCD is how these models break conformal symmetry. AdS/CFT stands for Anti-de Sitter/Conformal Field theory, which comes from the fact that the quantum field theory side possesses conformal symmetry. On the other hand, QCD has massive excitations and a running coupling, so it clearly does not possess conformal symmetry, except in its high energy limit. This means that in order for a holographic model to describe QCD, conformal symmetry will have to be broken. In black hole solutions, it turns out there is a mechanism which breaks this symmetry, namely the black hole horizon. Since the extra dimension can be identified with the energy scale, the horizon acts like an IR cutoff. This clearly breaks the conformal symmetry, and it turns out that it breaks supersymmetry as well. It is, however, a very crude way to break conformal symmetry, since it breaks it abruptly, which is not what happens in QCD.

The solution to this problem given by IHQCD is to introduce a dilaton with a non-trivial potential to replace the cosmological constant in other models[22,

25, 23, 24]. In the gravitational description this means that the action[14]

$$S_{\text{grav}} = M^3 N_c^2 \int \mathrm{d}^5x\sqrt{g}\left(\mathcal{R} + \frac{12}{R^2}\right),$$

in which $\mathcal{R}$ is the Ricci scalar and R is the AdS radius, is replaced by[26]

$$S_{\text{grav}} = M^3 N_c^2 \int \mathrm{d}^5x\sqrt{g}\left(\mathcal{R} - \frac{4}{3}\frac{(\partial\lambda)^2}{\lambda^2} + V_{\text{eff}}(\lambda)\right).$$

The potential V_{eff} is chosen so that near the AdS boundary the original action is recovered. This dilaton turns out to behave like a running coupling, and the potential V_{eff} now determines specifics of the model. Also note that the dilaton is identified with the 't Hooft coupling $\lambda = g^2 N_c$.

In order to have a theory consistent with QCD, it turns out that V_{eff} should satisfy several properties. Firstly it should be a monotonic function, and it should also have an expansion as follows in the UV, which corresponds to the AdS boundary at $r = 0$ or $\lambda = 0$[26]:

$$V_{\text{eff}}(\lambda) = \frac{12}{R^2}(1 + v_0\lambda + v_1\lambda^2) + \mathcal{O}(\lambda^3).$$

Since the dilaton behaves like the running coupling of QCD, we can match these coefficients to its beta function:

$$\beta(\lambda) = -b_0\lambda^2 - b_1\lambda^3 + \mathcal{O}(\lambda^4).$$

In this matching, one obtains

$$b_0 = \frac{9}{8}v_0, \qquad b_1 = \frac{9}{4}v_1 - \frac{207}{256}v_0^2.$$

These beta function coefficients will, through this potential, also enter in the near-boundary expansion of the solutions to our holographic model. In the IR, we want the theory to be confining. It turns out that this also doesn't happen for all asymptotics of V_{eff} as $\lambda \to \infty$. For the potentials in this paper, as can be seen in the results, this condition is satisfied.

A particular example of such a potential is given in [24]:

$$V_{\text{eff}}(\lambda) = \frac{12}{R^2}\left\{1 + V_0\lambda + V_1\lambda^{4/3}\left[\log\left(1 + V_2\lambda^{4/3} + V_3\lambda^2\right)\right]^{1/2}\right\}, \tag{1}$$

with

$$V_0 = \frac{8}{9}b_0, \qquad V_1 = 14, \qquad V_2 = b_0^4\left(\frac{23 + 36b_1/b_0^2}{81V_1}\right)^2, \qquad V_3 = 170,$$

and

$$b_0 = \frac{22}{3(4\pi)^2}, \qquad \frac{b_1}{b_0^2} = \frac{51}{121}.$$

With this potential, the model has three phases, namely one thermal gas phase, and two deconfined phases. Of the latter two, one is characterized by a small black hole, and the other by a big black hole. This distinction between two black hole phases is made because for each temperature there are multiple solutions,

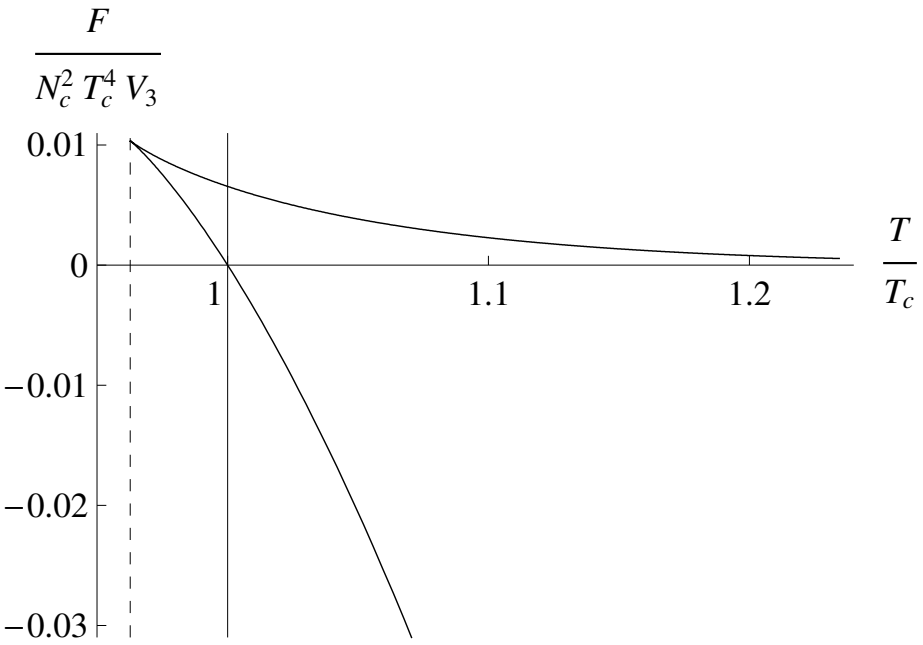

Figure 4: Free energy as a function of temperature in the IHQCD model described by (1). It can be seen that there are two branches. The branch with positive free energy for all T is the small black hole phase, while the branch which has negative free energy above $T = T_c$ is the big black hole phase.

as can be seen in figure 4. Since the thermal gas solution has no black hole, it can be approximated by the small black hole phase. This can be seen in figure 4, since the small black hole phase approaches zero free energy for large temperatures, which in this model and this phase corresponds to a shrinking black hole. Since the free energy is defined relative to the thermal gas solution, the figure also shows that the small black hole phase is never dominant. The big black hole phase is dominant above a critical temperature $T = T_c$, while below this temperature the thermal gas solution is dominant. Hence the phase diagram for this model is a deconfined phase above T_c, and a confined phase below T_c.

Studies show that the model discussed in the paragraph above agrees well with lattice data[36]. Examples of this are shown in figures 5, 6 and 7 for the energy density, entropy density, and pressure, respectively. In these figures, two

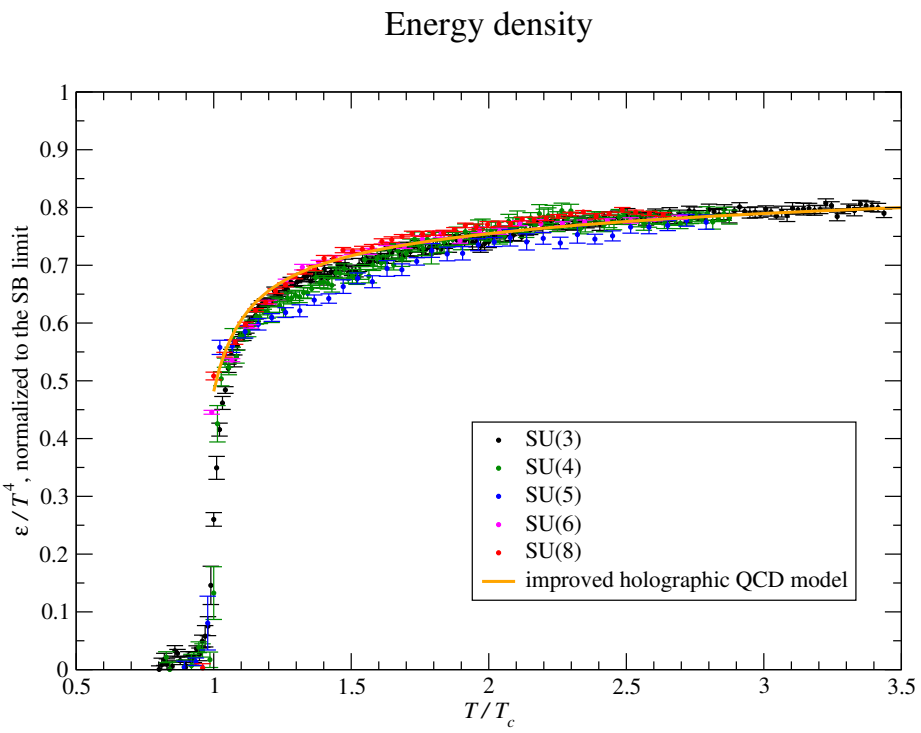

Figure 5: Energy density as a function of temperature, both for lattice data and the IHQCD model described by (1).

important observations can be made. The first is that the number of colors N_c used in the lattice simulation doesn't appear to influence the results much. This is an indication that the limit $N_c \to \infty$ still describes the qualitative behavior of QCD well. The second is that the IHQCD model discussed above appears to fit the lattice data very well. This indicates that it likely describes the glue sector of QCD well.

When flavor is introduced, the gravitational action typically gets a contri-

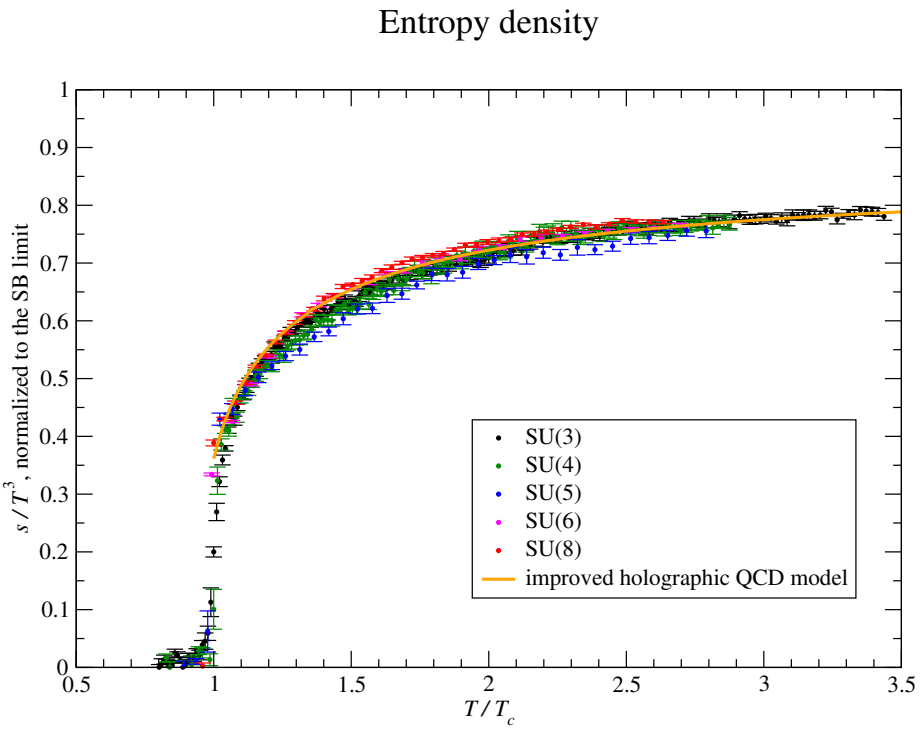

Figure 6: Entropy density as a function of temperature, both for lattice data and the IHQCD model described by (1).

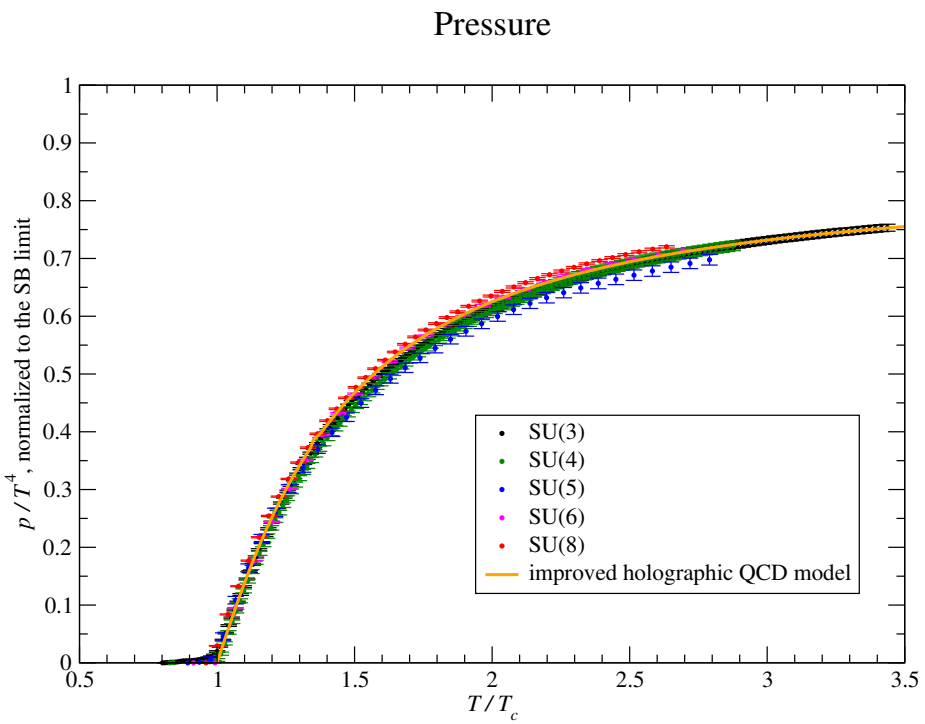

Figure 7: Pressure as a function of temperature, both for lattice data and the IHQCD model described by (1). Note that pressure is equal to minus the free energy.

bution from a Dirac-Born-Infeld (DBI) term[31, 3, 2]:

$$S_{\text{flavor}} = xM^3N_c^2 \int \mathrm{d}^5x\sqrt{g}V_f(\lambda,\tau)\sqrt{\det(g_{\mu\nu} + w(\lambda,\tau)V_{\mu\nu} + \kappa(\lambda,\tau)\partial_\mu\tau\partial_\nu\tau)},$$

where τ is a tachyonic field sourcing $\bar{q}q$, and $V_{\mu\nu}$ is an external potential. Also, $x = N_f/N_c$ is the ratio between the number of flavors and the number of colors. Also, there are a few new potentials, namely V_f, κ and w. These potentials can, just as V_{eff}, be matched to properties of QCD. Details on how V_f and κ can be chosen for $B = 0$ can be found in [3]. In this thesis, we chose w to match the result in figure 2.

The external potential can also be used to turn on a chemical potential. This has been done in [2]. There, they use the same potentials as the ones introduced in the next section, with the constant $C = 1$. This leads to the phase diagram in the (T, μ)-plane shown in figure 8. As can be seen, the model

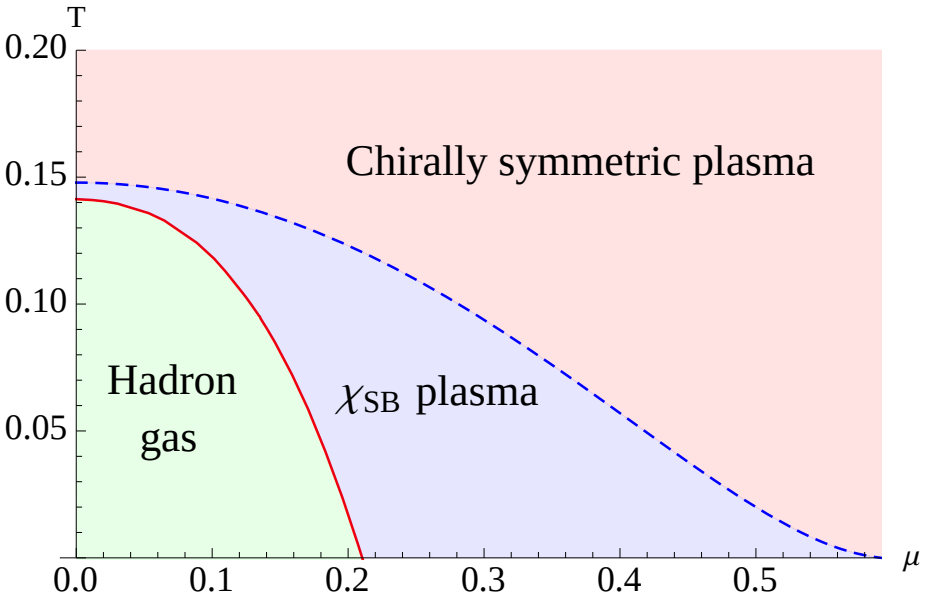

Figure 8: Phase diagram in the (T, μ)-plane for the IHQCD model in [2]. It can be seen that next to the deconfinement transition there is another transition within the deconfined phase.

has three distinct phases, but these are not the same phases as for the pure glue model. In this model, there is a thermal gas as before, which corresponds to the confined phase, and there are two black hole phases, both corresponding to a big black hole phase. As before, there are also small black hole phases, and they are again never dominant. The two black hole phases are distinguished by chiral symmetry, which is broken in the chirally broken phase, and unbroken in the chirally symmetric phase. As was discussed before, the chiral condensate is the order parameter of the chiral transition, so that we have $\langle\bar{q}q\rangle = 0$ in the chirally symmetric phase, and $\langle\bar{q}q\rangle \neq 0$ in the chirally broken phase.

4 The holographic model and its solutions

4.1 Action and equations of motion

The gravitational action of the Veneziano QCD model used in this thesis is a modification[6] of the one in [2] given by

$$S = M^3 N_c^2 \int \mathrm{d}^5x \left[\sqrt{g}\left(\mathcal{R} - \frac{4}{3}\frac{(\partial\lambda)^2}{\lambda^2} + V_g(\lambda)\right) - xV_f(\lambda,\tau)\sqrt{\det(g_{\mu\nu} + w(\lambda)V_{\mu\nu} + \kappa(\lambda)\partial_\mu\tau\partial_\nu\tau)}\right]. \tag{2}$$

Here the first term contains the fields dual to the gluon content of the theory, and the second part, which is a Dirac-Born-Infeld (DBI) action, contains the flavor content. Of the fields appearing in the action, $\lambda = e^\phi$ is the dilaton field, τ is a tachyon, and $V_{\mu\nu}$ is the electromagnetic field tensor, which is taken to be a constant magnetic field. Also, R is the Ricci scalar and $x = N_f/N_c$ is the ratio between the number of flavors and the number of colors. Note that from (2) it is clear that the scaling $w(\lambda) \mapsto Dw(\lambda)$ effectively scales $V_{\mu\nu}$, and hence B. The ansatz for the black hole vacuum solution of the metric is given by

$$\mathrm{d}s^2 = e^{2A(r)}\left(\frac{\mathrm{d}r^2}{f(r)} + f(r)\,\mathrm{d}t^2 + \mathrm{d}x_1^2 + \mathrm{d}x_2^2 + e^{2W(r)}\,\mathrm{d}x_3^2\right),$$

and the potential functions are given as in [2]:

$$V_g(\lambda) = 12\left[1 + \frac{88\lambda}{27} + \frac{4619\lambda^2}{729}\frac{\sqrt{1+\log(1+\lambda)}}{(1+\lambda)^{2/3}}\right],$$

$$xV_f(\lambda,\tau) = \left[W_0 + W_1\lambda + W_2\lambda^2\right]e^{-\frac{3}{2}\tau^2/\mathcal{L}_{\mathrm{UV}}^2},$$

$$\kappa(\lambda) = \frac{\left[1+\log(1+\lambda)\right]^{-1/2}}{\left[1+\frac{609-96x}{216}\lambda\right]^{4/3}}, \qquad w(\lambda) = \kappa(C\lambda),$$

with $C = 0.25$, and

$$\mathcal{L}_{\mathrm{UV}} = \left(1 + \frac{7x}{4}\right)^{1/3}, \qquad W_0 = 12\left(1 - \frac{1}{\mathcal{L}_{\mathrm{UV}}^2}\right),$$

$$W_1 = \frac{96}{27\mathcal{L}_{\mathrm{UV}}^2}\left(11\mathcal{L}_{\mathrm{UV}}^2 - 11 + 2x\right),$$

$$W_2 = \frac{12}{729\mathcal{L}_{\mathrm{UV}}^2}\left(4619\mathcal{L}_{\mathrm{UV}}^2 - 4619 + 1714x - 92x^2\right).$$

In the metric ansatz, there appears a factor of $\exp(2W)$, which, if non-zero, breaks rotational symmetry. This is exactly as expected, given that the magnetic field breaks it as well.

[6] It is the same action symbolically, but the expression for $V_{\mu\nu}$ is different in this case.

4.1.1 Equations of motion and on-shell action

There are six equations of motion, four of which come from the Einstein equations, and the other two come from the variations of the dilaton and the tachyon. Since there are only five degrees of freedom, one of these equations is superfluous, but this extra equation will still be needed to write the on-shell action in a simple form. Note that this derivation is a very lengthy one if done by hand, which makes mistakes likely. To make sure the equations below are correct, they have been computed both by hand and using Mathematica. Also, they have been compared to an independently computed derivation.

The Einstein equations yield

$$3\ddot{A} + \frac{2}{3}\frac{\dot{\lambda}^2}{\lambda^2} + 3\dot{A}^2 + (3\dot{A} - \dot{W})\frac{\dot{f}}{2f} + \frac{xV_f G e^{2A}}{2Qf}\left(2Q^2 - 1\right) - \frac{e^{2A}V_g}{2f} = 0, \tag{3}$$

$$\ddot{W} + \frac{\dot{W}\dot{f}}{f} + \dot{W}^2 + 3\dot{A}\dot{W} + \frac{xV_f G e^{2A}}{2Qf}\left(1 - Q^2\right) = 0, \tag{4}$$

$$\ddot{f} + (3\dot{A} + \dot{W})\dot{f} + \frac{xV_f e^{2A} G}{Q}\left(1 - Q^2\right) = 0, \tag{5}$$

$$\frac{2}{3}\frac{\dot{\lambda}^2}{\lambda^2} - (3\dot{A} + \dot{W})\frac{\dot{f}}{2f} - 6\dot{A}^2 - 3\dot{A}\dot{W} + \frac{e^{2A}V_g}{2f} - \frac{xV_f Q e^{2A}}{2Gf} = 0, \tag{6}$$

where a dot denotes a derivative with respect to r, and the arguments of the potential functions are omitted for brevity. In the above, the abbreviations

$$G = \sqrt{1 + e^{-2A}\kappa f \dot{\tau}^2}, \qquad Q = \sqrt{1 + w^2 B^2 e^{-4A}}$$

were used. Also note that the last of these four equations is the superfluous equation mentioned before. The dilaton and tachyon equations of motion are given by

$$\begin{aligned} 0 = {} & \frac{\ddot{\lambda}}{\lambda} - \frac{\dot{\lambda}^2}{\lambda^2} + \left(3\dot{A} + \dot{W} + \frac{\dot{f}}{f}\right)\frac{\dot{\lambda}}{\lambda} + \frac{3}{8}\frac{\lambda e^{2A}}{f}\partial_\lambda V_g \\ & - \frac{3xB^2 e^{-2A} G\lambda V_f w}{8fQ}\partial_\lambda w - \frac{3xe^{2A} G\lambda Q}{8f}\partial_\lambda V_f - \frac{3x\lambda Q V_f \dot{\tau}^2}{16G}\partial_\lambda \kappa, \end{aligned} \tag{7}$$

$$\begin{aligned} 0 = {} & \ddot{\tau} - \frac{e^{2A}G^2}{f\kappa}\partial_\tau \log V_f \\ & + e^{-2A} f\kappa\dot{\tau}^3\left(\dot{W} + \frac{\dot{f}}{2f} + 2\dot{A}\frac{1+Q^2}{Q^2} + \frac{\dot{\lambda}}{2}\partial_\lambda \log\left(\kappa V_f^2\right) - \frac{\dot{\lambda}\left(1-Q^2\right)}{Q^2}\partial_\lambda \log w\right) \\ & + \dot{\tau}\left(\dot{A}\frac{2+Q^2}{Q^2} + \dot{W} + \frac{\dot{f}}{f} + \dot{\lambda}\partial_\lambda \log(V_f\kappa) - \frac{\dot{\lambda}\left(1-Q^2\right)}{Q^2}\partial_\lambda \log w\right). \end{aligned} \tag{8}$$

From the AdS/CFT correspondence, we know that the Helmholtz free energy is proportional to the on-shell gravitational action. The latter can be computed in two simple steps. First, taking the trace of the Einstein's equations, we find that

$$\mathcal{R} = \frac{4}{3}\frac{(\partial\lambda)^2}{\lambda^2} - \frac{5}{3}V_g + \frac{2xV_f}{3}\left(\frac{G}{Q} + QG + \frac{Q}{2G}\right).$$

Using this, and recognizing that the square root appearing in (2) is equal to QG, one obtains

$$S_{\text{on-shell}} = M^3 N_c^2 \int \mathrm{d}^5 x e^{5A+W} \left[-\frac{2}{3} V_g + x V_f \left(\frac{2G}{3Q} - \frac{QG}{3} + \frac{Q}{3G} \right) \right].$$

Subsequently using equations(3–6) the potential functions can be eliminated, a Gibbons-Hawking term can be added, and the resulting expression then becomes

$$\begin{aligned} S_{\text{on-shell}} &= -2M^3 N_c^2 \beta V \int_0^{r_h} \frac{\partial}{\partial r} \left[e^{3A+W} f(\dot{A} + \dot{W}) \right], \\ &= 2M^3 N_c^2 \beta V e^{3A+W} f(\dot{A} + \dot{W}) \Big|_{r=0}. \end{aligned}$$

with r_h the location of the black hole horizon, β is the size of the compactified dimension and V is the volume of the 3 dimensional space. Because $\dot{A}$ diverges at the AdS boundary, it is clear that this expression will need to be regularized if it is to be used to obtain the free energy. This is why in the following a different method to obtain it will be employed. Note that the derivation of the on-shell action is another computation of mathematical interest.

Because the boundary coordinate singularity is numerically difficult to handle, the equations of motion are rewritten to use A as the independent variable using the auxiliary variable $q = e^A \partial r / \partial A$[2]. Equations (3–6) then transform to

$$6 - \frac{3q'}{q} + \frac{2}{3}\frac{\lambda'^2}{\lambda^2} + (3 - W')\frac{f'}{2f} + \frac{x V_f G q^2}{2Qf}\left(2Q^2 - 1\right) - \frac{q^2 V_g}{2f} = 0, \tag{9}$$

$$W'' + W'\left(4 - \frac{q'}{q} + \frac{f'}{f}\right) + W'^2 + \frac{x V_f G q^2}{2Qf}\left(1 - Q^2\right) = 0, \tag{10}$$

$$f'' + f'\left(4 - \frac{q'}{q} + W'\right) + \frac{x V_f G q^2}{Q}\left(1 - Q^2\right) = 0, \tag{11}$$

$$\frac{2}{3}\frac{\lambda'^2}{\lambda^2} - (3 + W')\frac{f'}{2f} - 6 - 3W' + \frac{V_g q^2}{2f} - \frac{V_f Q q^2}{2Gf} = 0, \tag{12}$$

respectively. Note that a prime denotes a derivative with respect to A, and that one now has

$$G = \sqrt{1 + \frac{\kappa f \tau'^2}{q^2}}.$$

The dilaton and tachyon equations (7–8) transform to

$$\begin{aligned} 0 = {} & \frac{\lambda''}{\lambda} - \frac{\lambda'^2}{\lambda^2} + \left(4 - \frac{q'}{q} + W' + \frac{f'}{f}\right)\frac{\lambda'}{\lambda} + \frac{3}{8}\frac{\lambda q^2}{f}\partial_\lambda V_g \\ & - \frac{3x B^2 e^{-4A} q^2 G \lambda V_f w}{8fQ}\partial_\lambda w - \frac{3xG\lambda Q q^2}{8f}\partial_\lambda V_f - \frac{3x\lambda Q V_f \tau'^2}{16G}\partial_\lambda \kappa, \end{aligned} \tag{13}$$

$$\begin{aligned} 0 = {} & \tau'' - \frac{q^2 G^2}{f\kappa}\partial_\tau \log V_f \\ & + \frac{f\kappa\tau'^3}{q^2}\left(W' + \frac{f'}{2f} + 2\frac{1+Q^2}{Q^2} + \frac{\lambda'}{2}\partial_\lambda \log\left(\kappa V_f^2\right) - \frac{\lambda'\left(1-Q^2\right)}{Q^2}\partial_\lambda \log w\right) \\ & + \tau'\left(1 - \frac{q'}{q} + \frac{2+Q^2}{Q^2} + W' + \frac{f'}{f} + \lambda'\partial_\lambda \log(V_f \kappa) - \frac{\lambda'\left(1-Q^2\right)}{Q^2}\partial_\lambda \log w\right). \end{aligned} \tag{14}$$

4.1.2 Expansion near the boundary

Near the boundary at $r = 0$, equations (3–6) and (8) lead to the following expansions:

$$A = \log \frac{\mathcal{L}_{\text{UV}}}{r} + \frac{4}{9\log(\Lambda r)} + \frac{\frac{1}{162}\left(95 - \frac{64V_2}{V_1^2}\right) + 81\log(-\log(\Lambda r))\left(-23 + \frac{64V_2}{V_1^2}\right)}{\log(\Lambda r)^2} + \mathcal{O}\left(\frac{1}{\log(\Lambda r)^3}\right), \tag{15}$$

$$\lambda = -\frac{8}{9V_1\log(\Lambda r)} + \frac{\log(-\log(\Lambda r))\left(\frac{46}{81} - \frac{128V_2}{81V_1^2}\right)}{\log(\Lambda r)^2} + \mathcal{O}\left(\frac{1}{\log(\Lambda r)^3}\right), \tag{16}$$

$$f = 1 + \frac{Cr^4}{4\mathcal{L}_{\text{UV}}^3} + \mathcal{O}\left(r^5\right), \qquad W = \frac{Dr^4}{4\mathcal{L}_{\text{UV}}^3} + \mathcal{O}\left(r^5\right), \tag{17}$$

$$\frac{\tau}{\mathcal{L}_{\text{UV}}} = m_q r\left(-\log(\Lambda r)\right)^{-\gamma_0/b_0} + \langle\bar{q}q\rangle r^3\left(-\log(\Lambda r)\right)^{\gamma_0/b_0}, \tag{18}$$

with Λ, C, D, γ_0/b_0, m_q and $\langle\bar{q}q\rangle$ integration constants and

$$V_1 = \frac{88 - 16x}{27}, \qquad \frac{V_2}{V_1^2} = \frac{1}{64}\left(23 + \frac{54(34 - 13x)}{(11 - 2x)^2}\right), \qquad \frac{\gamma_0}{b_0} = \frac{9}{22 - 4x}.$$

The constants m_q and $\langle\bar{q}q\rangle$ correspond to the quark mass and chiral condensate, respectively. These expansions will be used as boundary conditions in the next section. Also, note that these boundary expansions are identical to those in [3], which were computed for a different holographic model. Lastly, note that this is another result of mathematical interest.

4.2 Numerical solution to the equations of motion

To obtain solutions to the equations of motion, the equations need to be integrated numerically. This is done by means of the Dormand-Prince algorithm. This algorithm is $\mathcal{O}(h^5)$ accurate, where h is the step size. The step size itself is dynamically chosen by the algorithm to keep errors within a specified bound. Details on this method are given in appendix A.

Solutions to the equations of motion are subject to the near-boundary expansions (15–18). Since only black hole solutions will be considered, this is complemented by the condition that $f(r) = 0$ for some $r \in \mathbb{R}$. Also, quarks will be assumed massless, so that it is also required that $m_q = 0$. The exact method for making sure that these boundary conditions are satisfied can be found in appendix B.

One particular solution to the equations of motion is shown in figure 9. Once a solution has been obtained, the temperature is identified with the Hawking temperature of the 5-dimensional black hole, and the entropy is identified with its Bekenstein-Hawking entropy:

$$\frac{T}{\Lambda} = \frac{-\dot{f}_h}{4\pi}, \qquad \frac{S}{\Lambda^3} = \exp(3A_h + W_h).$$

The details on how this is done are given in appendix B. In this appendix it is also explained how m_q and $\langle\bar{q}q\rangle$ are extracted. As is noted in the figure, B is

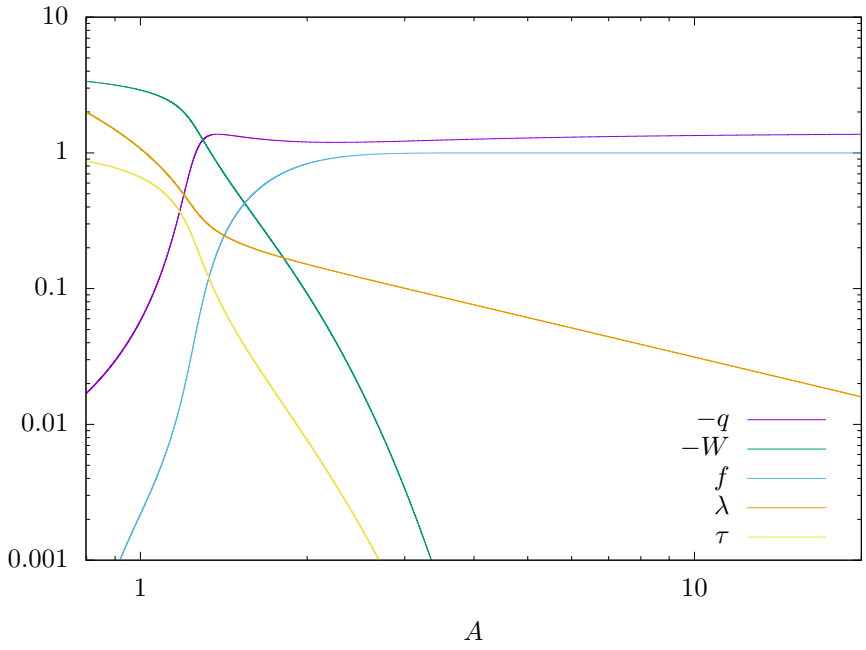

Figure 9: Solution to the equations of motion for $\lambda_h = 2$, $\tilde{B} = 3$ and $\tau_h = 0.873685$, where a subscript h indicates a value at the horizon. $\tilde{B}$ is an unphysical input parameter. Its precise definition is explained in appendix B. The thermodynamics extracted from this solution are $T/\Lambda = 0.0686755$, $S/\Lambda^3 = 0.37702$, $B/\Lambda^2 = 14.7928$.

also extracted, since this method does not give direct control over the value of B. Instead, the related value $\tilde{B}$ can be directly controlled. The relation between B and $\tilde{B}$, as well as the extraction of the former, are explained in appendix B.

4.3 Chiral transition

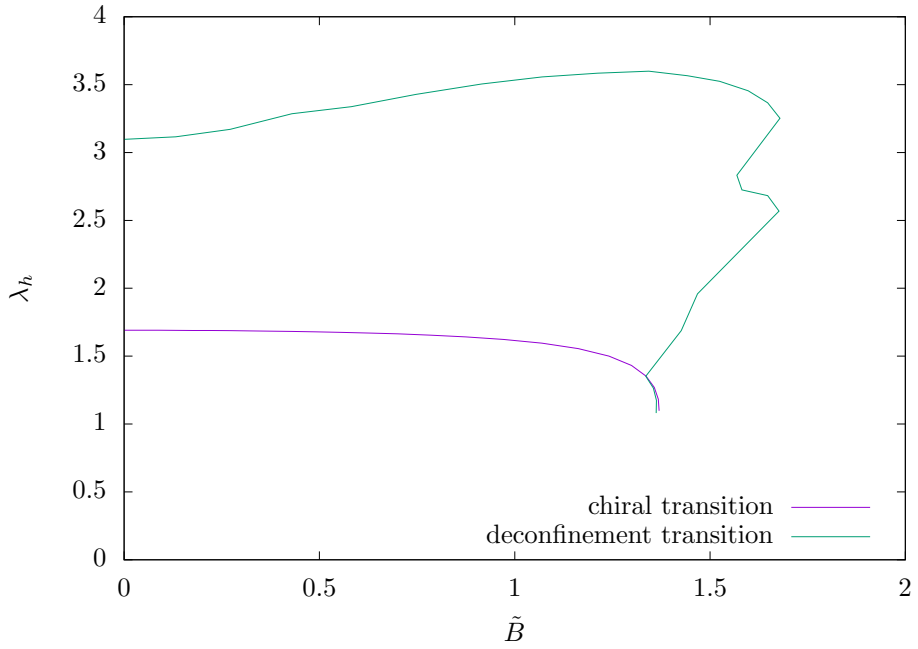

Figure 10: Location of both the chiral and the confining transition in the $(\lambda_h, \tilde{B})$-plane. Note that the deconfinement transition for large $\tilde{B}$ shows behavior which looks like it's not right. This behavior also causes the irregularities in figure 11. However the final result given in figure 11 has been cross-checked with a different method. It was found that for small $\tilde{B}$ there is good agreement, and for large $\tilde{B}$ there is at least qualitative agreement.

One of the boundary conditions is that $m_q = 0$. To realize this, note that the equations of motion imply that if $\tau_h = \dot{\tau}_h = 0$,[7] then $\tau = 0$ for all r. This yields the chirally symmetric solution. There also is the possibility of finding a $\tau_h \neq 0$ such that $m_q = 0$. This is called the chirally broken solution. The algorithm to find such a τ_h is given in appendix B.

For both these possibilities, note that there are only certain $(\lambda_h, \tilde{B})$-pairs which admit such a solution. It turns out that whenever multiple solutions exists, the free energy for the one with the largest τ_h is lower, so that the chirally broken phase dominates whenever it exists[2]. This implies that the chiral transition between the chirally broken and the chirally symmetric phase is given by the boundary of the area in the $(\lambda_h, \tilde{B})$-plane where the chiral solution exists. This line is given in figure 10, and the corresponding values for T and

[7] As can be seen in appendix B, $\tau_h = 0$ implies $\dot{\tau}_h = 0$ as well.

B are given in figure 11. The exact procedure used to obtain this transition is given in appendix C.

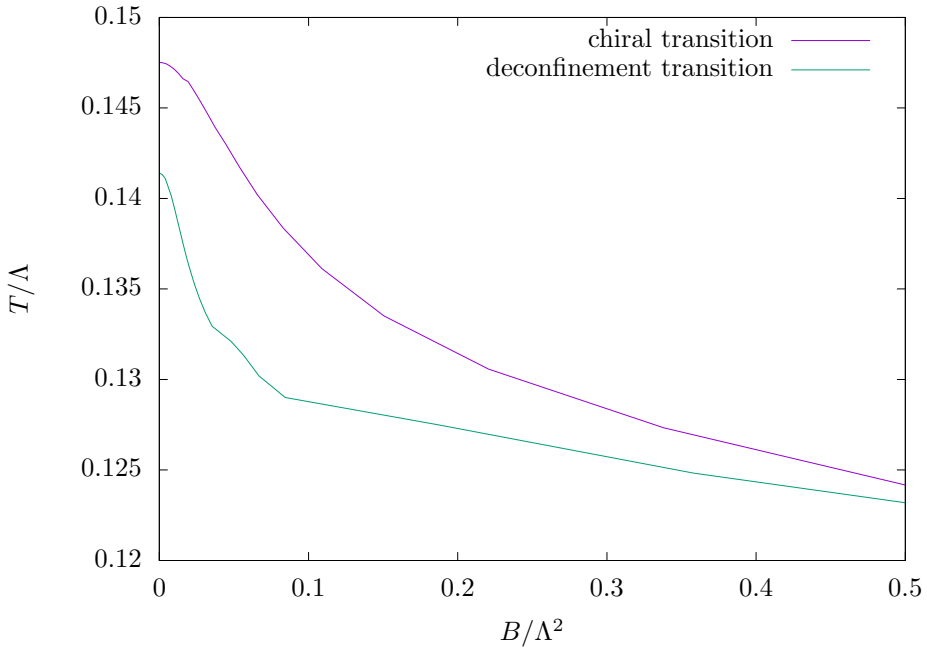

Figure 11: Chiral (T_χ) and confining (T_c) transition temperatures as a function of B. Note, as in figure 10, that there appears to be some numerical noise for large B. The result has been cross-checked with a different method though, and it is still in qualitative agreement.

4.4 Deconfinement transition

To find the confining transition, recall that the free energy of the confined phase is independent of temperature, and that the confined phase has the same geometry as a black hole solution in which the black hole is small, i.e. $\lambda_h \gg 1$. We can, however, not guarantee that the free energy of the confined phase is independent of magnetic field strength. This means that to determine whether a black hole solution is in the dominant phase, we need to compare its free energy to another black hole solution with the same B and $\lambda_h \gg 1$. This can be done by means of integrating the free energy $\mathrm{d}F = -S\,\mathrm{d}T$ along a line of constant B. The algorithm used to do this is described in appendix C, and by using this algorithm to find where $F = 0$, we find the confining transition. The result of this is shown in figures 10 and 11.

4.5 Phase diagram

Having calculated the two transitions in the system, it is possible to present the phase diagram. It turns out that chirally broken solutions exist only for temperatures below $T_\chi(B)$, and that the free energies of points below $T_c(B)$ are

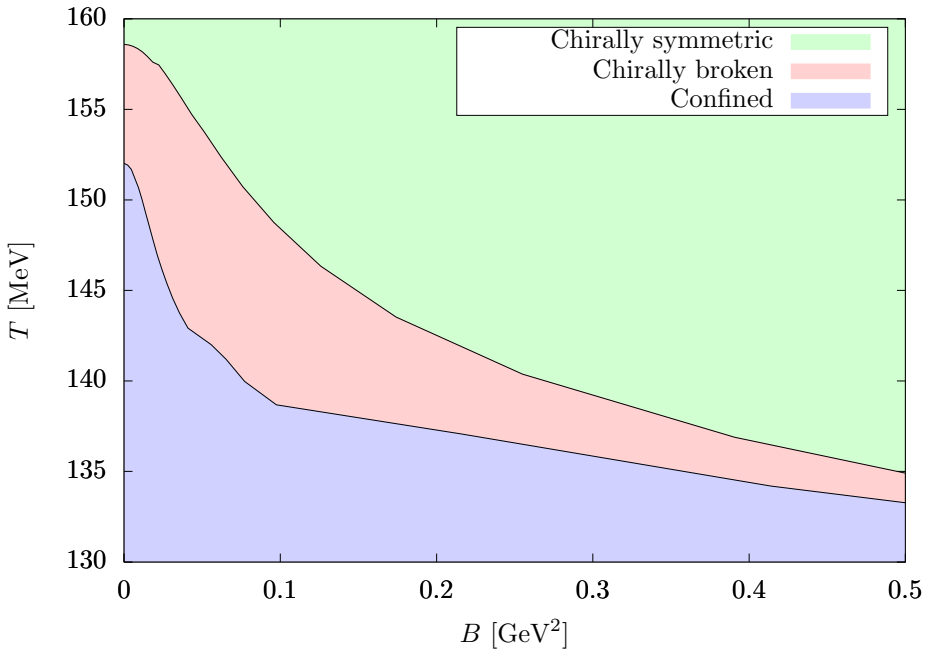

Figure 12: Phase diagram for this section's model. Note that Λ has been chosen in such a way that for $B = 0$ we get approximately $T_\chi = 159\,\text{MeV}$.

negative compared to their corresponding thermal gas solutions. This means that every point below $T_c(B)$ is in the confined phase, every point below $T_\chi(B)$ but above $T_c(B)$ is in the chirally broken phase, and every point above both transition temperatures is in the chirally symmetric phase. The resulting phase diagram is shown in figure 12. Note that in this figure, Λ has been chosen in such a way that the result agrees approximately with the lattice result of $T_\chi(B = 0) = 159\,\text{MeV}$. Note also that the shape of $T_\chi(B)$ is similar to that of the lattice result in figure 2. In particular, we indeed see that the magnetic field inversely catalyzes chiral symmetry breaking. The shape of $T_c(B)$ is similar to that of $T_\chi(B)$, so we can also conclude that the magnetic field inversely catalyzes hadronization.

The most striking difference between this result and the lattice result is that for the lattice result there is only one transition, because on the lattice it is found that the chiral- and deconfinement transitions occur at the same place. In this model this is clearly not the case. There are also holographic models [4] for which, if they are extended to incorporate an external magnetic field, there is only a deconfinement transition, but nevertheless it is still interesting to study this model, since in this model there is a deconfined chirally broken phase, in which it is possible to measure inverse magnetic catalysis of the chiral condensate directly, as can be seen in the next subsection. In the absence of a deconfined chirally broken phase, one can only study the chiral condensate in the confined phase. This can be done, but then temperature dependence of the chiral condensate is lost, in contrast to the lattice results. Another aspect in which the phase diagram disagrees with 2 is the scale of B, as the decrease of

the transition temperatures in our model occurs at smaller B than in the lattice result. As mentioned before, this can be easily changed by using the fact that the scaling $w(\lambda) \mapsto Dw(\lambda)$ effectively scales B. The reason why this has not been done is because such a change is incompatible with other known properties of QCD, which are outside the scope of this thesis.

4.6 Chiral condensate

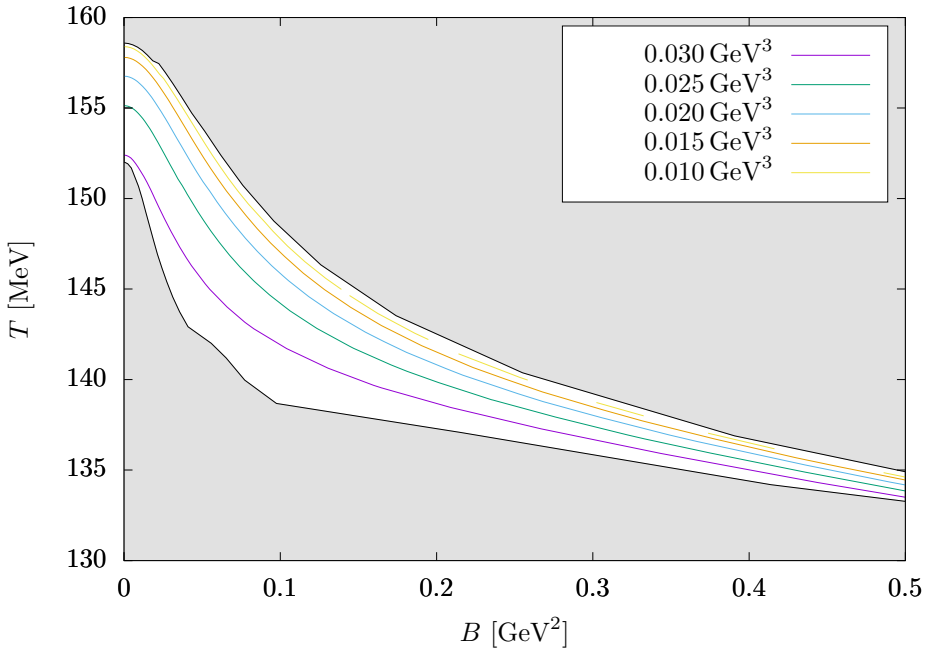

Figure 13: Contour plot of the chiral condensate of the chirally broken phase. Note that the condensate clearly decreases with increasing B. Also note that some of the contours near the chiral transition are not continuous. This is caused by the fact that this figure has been created by means of a grid, and near the chiral transition, points are missing from this grid, since on the other side of the transition the chirally broken solution doesn't exist. Because of this the contours near the chiral transition cannot be calculated everywhere. A solution would be to use a finer grid, but since the computational load scales with the squared inverse of the grid spacing this quickly becomes insurmountable. It took 3 days to compute this on a 50×50 grid, so to compute this on the next logical size, 100×100, would take almost 2 weeks.

Next to the phase diagram, there is also another interesting quantity which can be studied, namely the chiral condensate $\langle \bar{q}q \rangle$, which can be extracted by means of equation (18). The precise details on how this is done can be found in appendix B, and the result is shown in figure 13. In this figure, as was also seen in the chiral transition temperature, one can see that the chiral condensate is inversely catalyzed by the magnetic field. It can also be seen that it appears that the chiral condensate goes to zero near the chiral transition. This is confirmed

in figure 14, where $\langle \bar{q}q \rangle$ is shown on the chiral transition line. Note here that B has been used to parameterize this line. It can be seen that the condensate

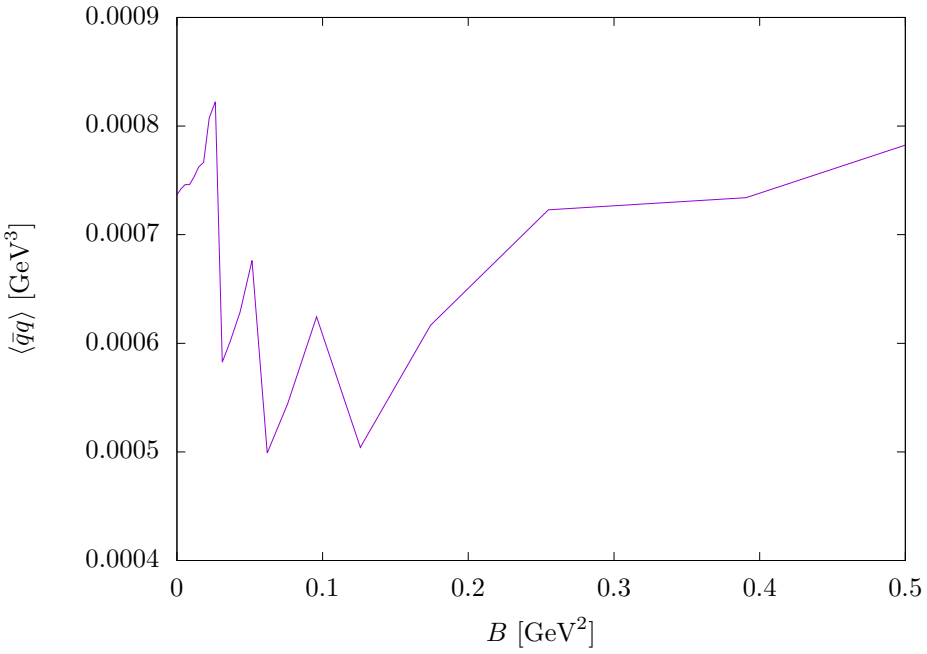

Figure 14: Chiral condensate of the chirally broken phase at the chiral transition. Note that this is close, but not equal, to zero.

is not exactly zero. However, it turns out that this is due to the fact that the algorithm described in appendix C only makes sure that we're close to the chiral transition, but how close exactly can be set by hand.

5 Conclusions and outlook

From our model we obtain a phase diagram in which there are two phase transitions. This might seem like a trivial statement, but there are also choices for the potentials[4] for which the chiral transition is not relevant because the black hole solutions at that transition have positive free energy compared to a thermal gas solution, which effectively hides the chiral transition. In the phase diagram (figure 12), it is clearly visible that both transition temperatures decrease as a function of magnetic field. In the case of the chiral transition, this means that we see inverse magnetic catalysis of the chiral condensate by the magnetic field, in agreement with the lattice model of [6]. This effect is also clearly visible in the chiral condensate as a function of T and B (figure 13). There we can see that if at fixed T we increase B, then the condensate becomes smaller. For the deconfinement transition, there is also agreement with the lattice results in a sense that the transition temperature decreases with increasing B. This is true since lattice results see that the two transitions occur at the same place. This means that we do see a decrease in transition temperature, but that it is not possible to

make both transitions match the lattice results at the same time. Summarizing these statements, the most important conclusion we can draw from this thesis is that we observe inverse magnetic catalysis in qualitative agreement between the holographic model and the lattice model of [6]. This means that we can answer the questions posed in the introduction affirmatively.

Another important thing to mention is the robustness of this result. Several things have been computed in more than one way, and this yielded similar answers in all cases. One example of this has already been given, namely the two different methods to compute the chiral condensate. However, one of our collaborators, Matti Järvinen, has computed the deconfinement transition in a different way, and found the same answer. With the introduction of the equations of motion it was also mentioned that the Helmholtz free energy needs renormalization before it can be used directly. This turned out to be too difficult to do numerically. The solution in this thesis has been to integrate a thermodynamical identity along a line of constant B, and there is a good reason for this. If $\mathrm{d}B \neq 0$, then the magnetization of the system appears in the integral, and the magnetization is also divergent, and needs to be renormalized. Our collaborator's solution has been to integrate along a straight line in the $(\lambda_h, \tilde{B})$-plane, taking the magnetization into account. This was possible because the magnetization diverges less than the free energy, and the result for the deconfinement transition turned out to be similar to the one found by the methods in this thesis. This, among other things, leads to the belief that the results are robust and can hence be trusted.

For future work, what could be done is to change some parameters in the potentials, and potentially use different potentials altogether, like for example the ones in [4]. For this thesis, we chose potentials which matched the lattice results best, but it is interesting to study what happens in different settings, to see whether inverse magnetic catalysis is only seen in this specific case, or that perhaps it is a general property of theories with an action of the form that we have taken. In line with this, it also makes sense to change the ratio $x = N_f/N_c$. As was mentioned before, there is no sound argument why it should be set to unity, so different values would be an interesting target of future research. Lastly, there is something that this thesis has not looked at, and that is the excitations of the vacuum. As was mentioned in the introduction, interesting things may happen to the excitations as a magnetic field is applied. This, too, could be a direction of future study.

6 Acknowledgements

I would like to first thank Umut and Yuri for their supervision and advice, and also my parents, friends and girlfriend for their support.

A Dormand-Prince method

To solve various differential equations found throughout this thesis, the Dormand-Prince (DP) method was employed. This is a fifth order Runge-Kutta method with adaptive step size. In general, such methods can be used to solve non-linear

ODEs with initial conditions of the form

$$\dot{y} = f(t, y), \qquad y(t_0) = y_0,$$

where y is a vector and f is smooth. Note that higher order ODEs can always be written in this form by introducing extra variables equal to the derivatives. As an example, the ODE given by $\ddot{x} = f(x) + g(\dot{x})$ can be written as

$$\begin{pmatrix} \dot{z} \\ \dot{x} \end{pmatrix} = \begin{pmatrix} f(x) + g(z) \\ z \end{pmatrix}.$$

A Runge-Kutta (RK) method is a generalization of the explicit Euler method, where $y_n := y(t_n)$ is given by the following iterative approximation:

$$y_{n+1} = y_n + hf(t_n, y_n),$$

with h the step size. RK methods use a more sophisticated approximation, namely

$$y_{n+1} = y_n + h \sum_{i=1}^{o} b_i k_i,$$

with o the number of stages of the RK method and

$$k_i = f\left(t_n + c_i h, y_n + h \sum_{j=1}^{i-1} a_{ij} k_j\right).$$

Here, b_i, c_i and a_{ij} are coefficients specific to the particular RK method used. These coefficients can be matched to an o-th order polynomial which solves the differential equation to order $\mathcal{O}(h^n)$, with n the order of the method, and if the coefficients match this solution, the RK method will approximately solve the differential equation. In our case, f is a very complicated function, so we can assume that most of the CPU time will be spent on evaluating it. In this approximation, an o-th order RK method will take about o times as long for a single step as the Euler method, which is in effect a 1st order RK method. As it turns out, if the RK coefficients are well chosen, an o stage RK method will be a lot more accurate then the Euler method with a step size o times as small. This is the main reason for using an RK method: for any required accuracy, the RK method will take less time than the Euler method.

The DP method is a fifth order RK method with adaptive step size. How this works is essentially that the DP method has two sets of coefficients b_i, the second of which we call b'_i. As mentioned before, both these sets of coefficients are chosen such that the RK method based on them approximately solves the differential equation, and since these two sets produce two different values for y_{n+1}, the difference Δy_{n+1} between those values can be taken as an error estimate. The values for b_i and b'_i are chosen with this in mind. The first set, b_i, solves the differential equation locally to order $\mathcal{O}(h^5)$, and yields the most accurate of the two estimates. The second set, b'_i, solves the differential equation locally only to order $\mathcal{O}(h^4)$, and is less accurate. Also, the first set is optimized so that its local truncation error is minimal. Because of this, the estimate obtained from b_i is taken to be the next estimate, and b'_i is purely used for the

error estimation. More about the derivation of these coefficients can be found in [19].

As mentioned earlier, the error estimate is taken to be the difference Δy_{n+1} between the two computed values for the next iteration. To determine whether the step size should increase or decrease, the following number is computed:

$$s = \sqrt[4]{\frac{h\epsilon}{2|\Delta y_{n+1}|}},$$

with ϵ the user-specified error tolerance per unit t. This means that if, for instance, we integrate the equation from $t = 0$ to $t = 1$, we expect an error no greater than ϵ. If our y is a vector, s is computed for each component, and the minimum is taken to reflect the error in the worst variable.[8] Then, the DP algorithm behaves differently based on the value of s:

- If $s < 1$, the error is outside the tolerances, so we reject the current step, halve the step size, and try again.
- If $1 \leq s < 2$, the error is within tolerances, so we accept the current step, and leave the step size untouched.
- If $s \geq 2$, the error is well within tolerances, so we accept the current step, and double the step size.

This approach has two distinct advantages over a fixed step size: The first is that in places where the variables change a lot, the step size automatically decreases to make sure no accuracy is lost. The second is that in places where there is not much happening, the computer is not wasting CPU time computing steps with a smaller step size than needed. Therefore we get the best of both worlds: speed and accuracy.

k	b_k	b'_k	c_k
1	35/384	5179/57600	0
2	0	0	1/5
3	500/1113	7571/16695	3/10
4	125/192	393/640	4/5
5	-2187/6784	-92097/339200	8/9
6	11/84	187/2100	1
7	0	1/40	1

Table 2: Numerical values for c_k, as well as both b_k and b'_k.

The coefficients of the DP method are given in tables 2 and 3. Note that k_7 is equal to k_1 of the next step, and that we don't have to evaluate f any extra times to get the error estimation. This means that we use in essence six evaluations per step.

[8] Note that in general one could make ϵ different for each variable. However, in this analysis, this was not done for simplicity.

$i\backslash j$	1	2	3	4	5	6
2	1/5					
3	3/40	9/40				
4	44/45	-56/15	32/9			
5	19372/6561	-25360/2187	64448/6561	-212/729		
6	9017/3168	-355/33	46732/5247	49/176	-5103/18656	
7	35/384	0	500/1113	125/192	-2187/6784	11/84

Table 3: Numerical values for a_{ij}.

B Numerical Method

B.1 Boundary conditions

As was previously mentioned, solutions must satisfy boundary conditions both at the horizon, where $f = 0$ by definition, and at the AdS boundary, where the geometry must be asymptotically AdS. On top of this, we need a way to parameterize solutions. One of the variables used for this is λ_h, or the value of the dilaton at the horizon. These requirements present us with a problem: To solve the differential equations, we need a point to start the computation from, and at this point the vector $y(t_0)$ from appendix A, which contains q, W, W', f, f', λ, λ', τ and τ', must be completely specified. We have boundary conditions at both ends of the region where the solution is to be computed, but at neither end do the conditions completely specify the required variables. On top of this, the equations of motion (9–14) contain f in the denominator in multiple places, potentially preventing the solution from being regular at the horizon.

The solution to both of these problems is to use symmetries of the equations of motion. It is easily seen that (9–14) are invariant under the following symmetries:

- Scaling of f:
$$f \to \frac{f}{\delta_f^2}, \qquad q \to \frac{q}{\delta_f},$$
- Shift of A:
$$A \to A + \delta_A, \qquad B \to Be^{2\delta_A},$$
- Shift of W:
$$W \to W + \delta_W.$$

It turns out that the requirement that the geometry must be asymptotically AdS, i.e. that for large A the expansions (15–18) hold true, can be satisfied by using these symmetries. Since the symmetries leave the equations of motion invariant, regularity at the horizon is preserved, as is the boundary condition that $f = 0$ at the horizon. One can also see that λ_h is preserved under the symmetries. This is the reason why we use it to parameterize solutions. However, it is also evident that the magnetic field is not invariant under the transformations, which explains the earlier statement that we don't have direct control over it.

The procedure to obtain a solution is hence as follows:

1. Enforce boundary conditions at the horizon setting λ_h by choice, and also choosing the magnetic field equal to $\tilde{B}$. These two quantities parameterize the solutions. In figure 10, it can be seen for which choices of $(\lambda_h, \tilde{B})$ the phase transitions occur. These can therefore be considered as typical values, but it must be noted that for the computation of the deconfinement transition much larger values for λ_h (typically 50) are needed. After setting λ_h and $\tilde{B}$, τ_h is set to either 0 if we want a chirally symmetric solution, or it is set to a specific non-zero value if we want a chirally broken solution. How this value is determined is detailed in the next subsection. In the latter case, we get $m_q \neq 0$ in general, and with the algorithm in the next subsection we can choose τ_h in such a way that $m_q = 0$. After setting $\tilde{A}_h = 0$, $\tilde{f}_h = 0$, $\tilde{f}'_h = 1$ and $\tilde{W}_h = 0$,[9] the other boundary conditions are set by requiring regularity as follows:

$$\tilde{q}_h = -\sqrt{\frac{3\tilde{f}'_h}{V_g(\lambda_h) + \frac{V_f(\lambda_h,\tau_h)}{2\tilde{Q}_h}(3 - 5\tilde{Q}_h^2)}},$$

$$\tilde{W}'_h = \frac{V_f(\lambda_h,\tau_h)\tilde{q}_h^2}{2\tilde{Q}_h\tilde{f}'_h}\left(1 - \tilde{Q}_h^2\right),$$

$$\lambda'_h = \frac{3\tilde{q}_h^2\lambda_h^2}{8f'_h}\left(\frac{\tilde{B}^2 V_f(\lambda_h,\tau_h)w(\lambda_h)}{\tilde{Q}_h}\frac{\partial w(\lambda_h)}{\partial\lambda} + \tilde{Q}_h\frac{\partial V_f(\lambda_h,\tau_h)}{\partial\lambda} - \frac{\partial V_g(\lambda)}{\partial\lambda}\right),$$

$$\tau'_h = \frac{\tilde{q}_h^2}{\tilde{f}'_h\kappa(\lambda_h)}\frac{\partial \log V_f(\lambda_h,\tau_h)}{\partial\tau},$$

with

$$\tilde{Q}_h = \sqrt{1 + w\left(\lambda_h\right)^2\tilde{B}^2}$$

2. Use the DP algorithm to obtain a solution $\{\tilde{q}, \tilde{W}, \tilde{f}, \tilde{\lambda}, \tilde{\tau}\}$, which is computed up to some large value $A_{\max}$. Note that this is where the notation $\tilde{B}$ originates, namely that it is the magnetic field of the solutions which have not yet been rescaled. Such a solution is given in figure 15.

3. Use the symmetries to rescale the solution so that it satisfies the boundary conditions at the AdS boundary. The new solution will be denoted the same as the old one, but without the tildes. In particular, this means that to obtain $f_{\max} = 1$ we apply scaling of f by $\delta_f = \sqrt{\tilde{f}_{\max}}$, where a subscript 'max' denotes evaluation at $A_{\max}$. The required shift of W to obtain $W_{\max} = 0$ is $\delta_W = -\tilde{W}_{\max}$.

   To compute the required shift in A is a bit less obvious. To do this, one needs to substitute equation (16) into (15) to obtain the following:

$$A = \log(\mathcal{L}_{\mathrm{UV}}\Lambda) + \frac{1}{b_0\lambda} + \frac{b_1}{b_0^2}\log(b_0\lambda) + \mathcal{O}(\lambda),$$

   with

$$b_0 = \frac{9V_1}{8}, \qquad \frac{b_1}{b_0^2} = \frac{16}{9}\left(\frac{V_2}{V_1^2} - \frac{23}{64}\right).$$

[9] Setting $\tilde{A}_h = 0$, $\tilde{f}'_h = 1$ and $\tilde{W}_h = 0$ is arbitrary, as these values will eventually be set by the symmetries anyway.

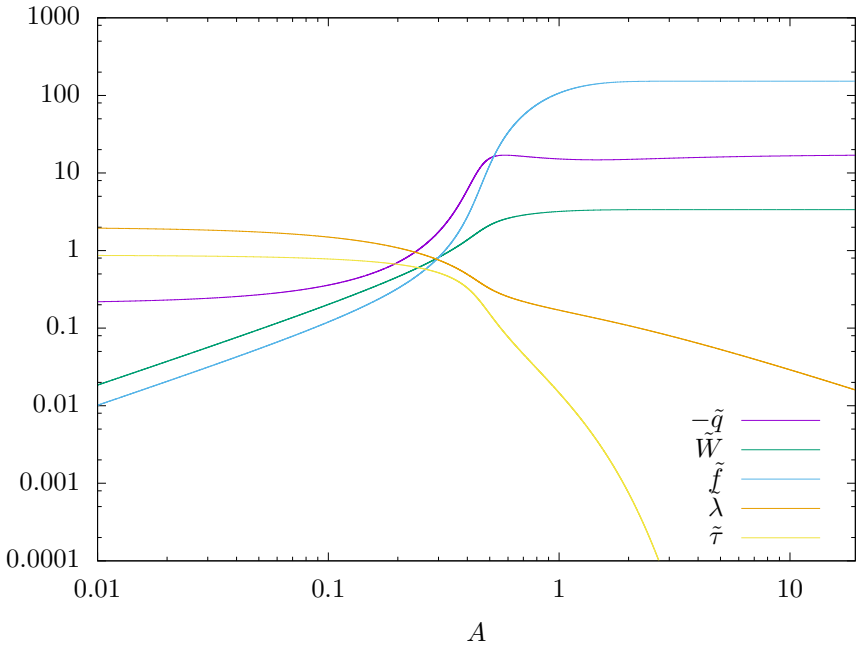

Figure 15: Solution to the equations of motion before rescaling, for the same λ_h, $\tilde{B}$ and τ_h as in figure 9. Note that the boundary conditions at the AdS boundary are not yet satisfied. This is particularly clear for f, which clearly doesn't equal 1 at large A.

Since λ is invariant under a shift in A, it becomes clear that we need

$$\delta_A = -\tilde{A}_{\max} + \log(\mathcal{L}_{\mathrm{UV}}\Lambda) + \frac{1}{b_0\lambda_{\max}} + \frac{b_1}{b_0^2}\log(b_0\lambda_{\max}).$$

This procedure can improved slightly by extrapolating $A_{\max} \to \infty$, which is the same limit as $\lambda_{\max} \to 0$. The way this is done is simply by calculating δ_A by the above formula for both $A_{\max}$ and $0.9A_{\max}$. We'll denote the corresponding values for δ_A by $\delta_{A_{\max}}$ and $\delta_{A_{0.9\max}}$, and the improved δ_A is then given by linear extrapolation:

$$\delta_{A,improved} = \delta_{A_{\max}} - \lambda_{\max} \cdot \frac{\delta_{A_{\max}} - \delta_{A_{0.9\max}}}{\lambda_{\max} - \lambda_{0.9\max}}. \tag{19}$$

In figure 16, one can see that indeed such a linear extrapolation is valid, since near $\lambda_{\max}$ the graph is linear.

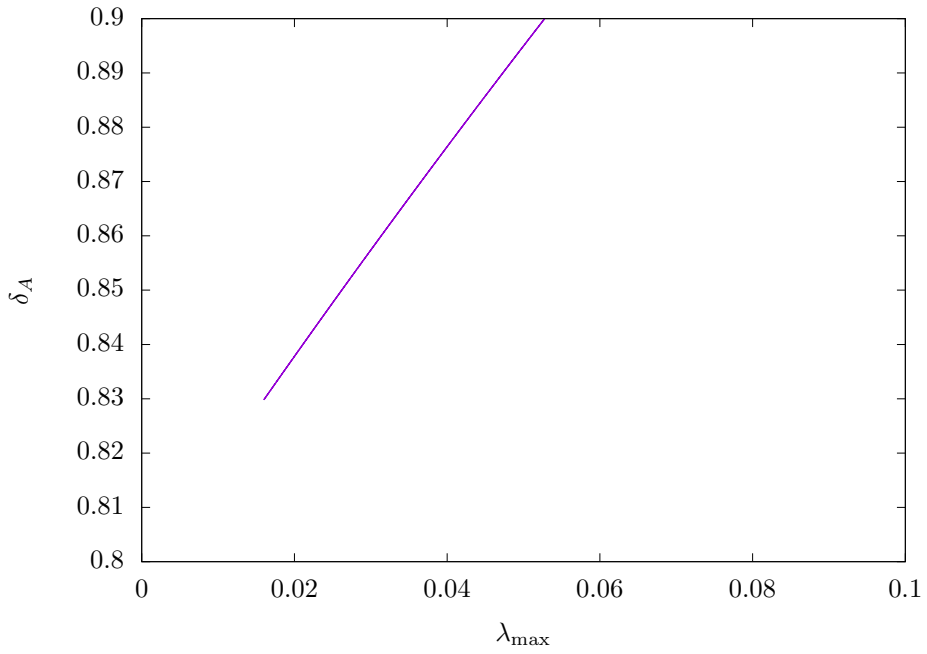

Figure 16: δ_A viewed as a function of $A_{\max}$, and plotted against $\lambda_{\max}$. One can see that the graph is linear, so that linear extrapolation likely works well.

By applying these three transformations, the solution in figure 9 is obtained, which satisfies all required boundary conditions. Note that it also satisfies $m_q = 0$, and how that is guaranteed is explained in the next subsection.

B.2 Setting quark mass to zero

The energy of the QCD scale is much larger than the mass of the quarks participating in the interactions. This means that to be representative of QCD,

the quark mass in this model should be set to zero. There are two ways to do this:[10]

- Set $\tau_h = 0$. This ensures that $\tau = 0$ for all A, so that $m_q = 0$. This choice corresponds to a phase in which chiral symmetry is not broken.
- Set τ_h to the largest possible non-zero value such that $m_q = 0$. This corresponds to a phase in which chiral symmetry is broken.

Note that neither of these solutions is guaranteed to exist at every $(\lambda_h, \tilde{B})$-pair. For the chirally symmetric solution, it is possible that asymptotes appear before the AdS boundary is reached, and for the chirally broken phase it is possible that there exist no non-zero τ_h such that $m_q = 0$.

From the main portion of this thesis, it is known that it is required to find the largest τ_h such that $m_q = 0$ to get the most stable phase. To check for the existence of a chirally symmetric solution, one can simply check whether setting $\tau_h = 0$ reaches the AdS boundary without encountering any asymptotes. One can subsequently check for the existence of chirally broken solutions by the following steps, which automatically find the largest τ_h such that $m_q = 0$[2]:

1. Start at $\tau_h = 1$, and check to see if there is a solution. If there is no solution, double τ_h and try again. Repeat this step until a solution is found, and define $\tau_{\text{exists}} = \tau_h$ at this point.
2. Do a binary search in the interval $[0, \tau_{\text{exists}}]$ to find a τ_h such that $m_q < 0$. Define $\tau_{\text{min}} = \tau_h$ at this point. After a number of such steps (20 in this thesis), the algorithm gives up and concludes there doesn't exist such a τ_{min}. This automatically means that the chirally broken solution doesn't exist for this $(\lambda_h, \tilde{B})$-pair.
3. Starting at τ_{min}, double τ_h until a τ_h is found such that $m_q > 0$. Define $\tau_{\text{max}} = \tau_h$ at this point.
4. Now a zero of $m_q(\tau_h)$ is guaranteed to exist in the interval $[\tau_{\text{min}}, \tau_{\text{max}}]$. This step checks that it is the largest such zero. First define the step length $\Delta\tau_h = \tau_{\text{min}}((\frac{\tau_{\text{max}}}{\tau_{\text{min}}})^{10^{-4}} - 1)$. Then the following is repeated until it is found that m_q rises exponentially as a function of τ_h.
   (a) Compute $y_1 = m_q(\tau_{\text{min}})$, $y_2 = m_q(\tau_{\text{min}} + \Delta\tau_h)$ and $y_3 = m_q(\tau_{\text{min}} + 2\Delta\tau_h)$. Before checking for zeroes, τ_{min} is incremented by $2\Delta\tau_h$ for the next iteration.
   (b) If the three values for m_q don't all have the same sign, a zero has been found, and the two values for τ_h bracketing the solution are saved. Also, the step length is updated to be the distance between the two values for τ_h bracketing the solution, divided by 5.
   (c) If no zero is found, fit a parabola through the three points. If this parabola has zeroes, update the step length to be the distance between these zeroes. If not, double the step size.[11]

[10] How exactly the quark mass is extracted from the solutions is detailed in the next subsection. This information, however, is not needed to understand this subsection.

[11] This departs from the procedure in [2], and is done to speed the computation up. I haven't observed any cases where this results in missed solutions, which justifies this change.

The iteration is stopped once the following conditions are met in a single step:

- $y_3 > 0$,
- $y_3 > y_1$,
- $y_3 > 100C$, where C is the largest m_q computed in any previous step.

5. Having two values for τ_h which bracket the largest zero, Brent's algorithm is guaranteed to find the correct root.

Note that within this algorithm there are several arbitrary choices made to ensure a good balance between accuracy and speed. Taking as an example the number of steps after which the search for $\tau_{\min}$ is abandoned, we might imagine that after 30 steps, we would have found a solution if we hadn't stopped after 20 steps. After experimenting with these values to see how they influence the results, it looks like these settings are good, providing both sufficient speed and sufficient accuracy. Another speed improvement made has to do with the accuracy setting of the Dormand-Prince algorithm. It turns out that the result doesn't change appreciably if, during steps 1–3 of the above listing, a lower accuracy setting is used. This speeds these three steps up dramatically, and can be felt especially in cases where we're not interested in the full computation, but only on the question of whether a chirally broken solution exists for a given $(\lambda_h, \tilde{B})$-pair. Examples of this can be found in appendix C.

B.3 Extraction of thermodynamical quantities

Of the thermodynamical quantities, the temperature, entropy and magnetic field are easiest to extract. Recall that the temperature equals the Hawking temperature of the black hole, i.e.:

$$\frac{T}{\Lambda} = \frac{-\dot{f}_h}{4\pi} = \frac{-f_h' \exp(A_h)}{4\pi q} = \frac{-\tilde{f}_h' \exp(\tilde{A}_h + \delta_A)}{4\pi \tilde{q}_h \delta_f} = \frac{-\exp(\delta_A)}{4\pi \tilde{q}_h \delta_f},$$

where it turns out everything can be written in terms of unrescaled quantities at the horizon and the AdS boundary. This is true for all quantities we'll extract, and it is an important point, because it means that we don't need to save the entire solution for the extraction of these quantities. This ensures that the whole process is very memory friendly. The entropy is given by the Bekenstein-Hawking entropy, i.e.:[12]

$$\frac{S}{\Lambda^3} = \exp(3A_h + W_h) = \exp(3\tilde{A}_h + 3\delta_A + \tilde{W}_h + \delta_W) = \exp(3\delta_A + \delta_W).$$

For the magnetic field, recall that we didn't have direct control over the magnetic field, but rather we were able to set $\tilde{B}$, the unrescaled magnetic field. To compute the real magnetic field, we simply rescale $\tilde{B}$:[13]

$$\frac{B}{\Lambda^2} = \tilde{B} e^{2\delta_A}.$$

[12] It is actually proportional to this value, but for all results in this thesis this proportionality constant will be unimportant.

[13] Note that the factor Λ^2 appears in the computation of δ_A.

The other quantities, namely the quark mass m_q and the chiral condensate $\langle\bar{q}q\rangle$, are harder to extract. Both are extracted from (18) with the help of (15). For m_q, we can ignore the $\langle\bar{q}q\rangle$ term in (18) since the m_q term dominates more and more as $A \to \infty$. Making this approximation and using $A = \log(\mathcal{L}_{\mathrm{UV}}/r)$ as an approximation of (15),[14] we obtain

$$\begin{aligned}\tau &= m_q \mathcal{L}_{\mathrm{UV}}^2 e^{-A} \left(A - \log(\mathcal{L}_{\mathrm{UV}}\Lambda)\right)^{-\gamma_0/b_0}, \\ &= m_q \mathcal{L}_{\mathrm{UV}}^2 e^{-\tilde{A}-\delta_A} \left(\tilde{A} + \delta_A - \log(\mathcal{L}_{\mathrm{UV}}\Lambda)\right)^{-\gamma_0/b_0},\end{aligned}$$

where this identity is valid in the limit $A \to \infty$. From it, we can extract m_q:

$$m_q = \lim_{A\to\infty} \tau \mathcal{L}_{\mathrm{UV}}^{-2} e^{\tilde{A}+\delta_A} \left(\tilde{A} + \delta_A - \log(\mathcal{L}_{\mathrm{UV}}\Lambda)\right)^{\gamma_0/b_0}.$$

In practice, this limit is computed by means of computing the expression in the limit both for $A = A_{\max}$ and for $A = 0.9A_{\max}$, and using an extrapolation method analogous to the one used in (19). Figure 17 is analogous to figure 16, but now for m_q instead of δ_A. Here the situation is not as clear as in figure 16,

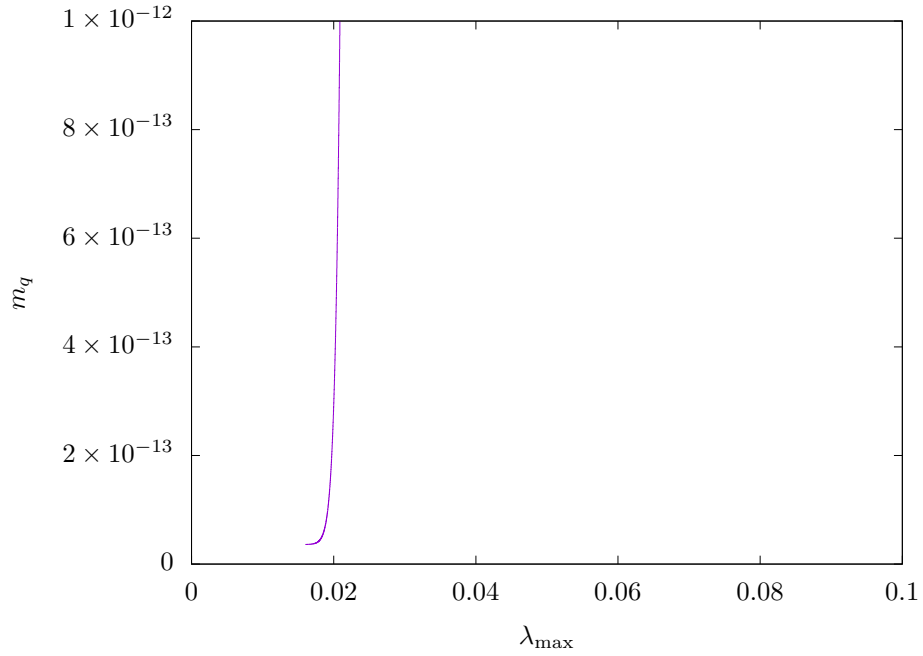

Figure 17: m_q as a function of $A_{\max}$, plotted against $\lambda_{\max}$. One can see that the graph is not perfectly linear near its end point.

since it is not clear that the graph is linear. This is no coincidence however, since this this plot satisfies the boundary condition that $m_q = 0$. This means that the cubic $\langle\bar{q}q\rangle$ term is important, and destroys linearity. However, it is clear from this figure that we have succeeded in finding a τ_h such that $m_q \approx 0$, since clearly the graph levels off near 0.

[14] This is a good approximation for $A \to \infty$.

The extraction of the chiral condensate requires a bit more thought. We cannot just use the same method as in the previous paragraph on the $\langle\bar{q}q\rangle$ term, since the m_q term dominates. Recalling that one of our boundary conditions is that $m_q = 0$, this may sound strange, but of course it is numerically impossible to make sure that m_q is *exactly* equal to zero by the method described in the previous paragraph, since in the end it relies on approximating a zero of a function. In practice we can only get it to be very small, but then still it prohibits a simple extraction of the condensate. There are two ways around this. The first relies on the fact that a bit further from the AdS boundary, the $\langle\bar{q}q\rangle$ term dominates, and there it can be matched to a second solution. This second solution is computed from the boundary, enforcing $m_q = 0$ exactly. Close to the AdS boundary, the τ equation decouples from the others and becomes approximately linear. This allows for the matching mentioned above. More details on this precise procedure can be found in appendix E of [3]. The second way to solve this problem is to divide by the term multiplying m_q so that m_q appears in the equation as a constant. This then allows for the removal of m_q entirely through differentiation, and the resulting equation can be rearranged to yield the following expression for $\langle\bar{q}q\rangle$:

$$\begin{aligned}\langle\bar{q}q\rangle = \lim_{A\to\infty} &\frac{\exp(2A)\left(A - \log(\mathcal{L}_{\mathrm{UV}}\Lambda)\right)^{-\gamma_0/b_0}}{2\mathcal{L}_{\mathrm{UV}}^3\left(\frac{\gamma_0}{b_0} - A + \log(\mathcal{L}_{\mathrm{UV}}\Lambda)\right)} \\ &\times\left[\exp(A)\left(\frac{\gamma_0}{b_0} + A - \log(\mathcal{L}_{\mathrm{UV}}\Lambda)\right)\tau + \mathcal{L}_{\mathrm{UV}}(-A + \log(\mathcal{L}_{\mathrm{UV}}\Lambda))\tau'\right].\end{aligned}$$

After making the substitution $A \to \tilde{A} + \delta_A$, this can be written in terms of the unrescaled solution, and the limit can be evaluated by the same extrapolation method as before. As before, a plot showing this extrapolation is shown in figure 18. It can be seen that this figure, too, is not perfectly linear. As in figure 17, this is due to the presence of the other term, namely the m_q term. Near $\lambda = 0$ the m_q term dominates and causes the deflection. The solution to this used in this thesis is to extrapolate from the linear part.

The two methods mentioned above have been compared, and for the potentials in this thesis they agree to within 10%, where the 10% appears to be an overall factor. This means that at least for qualitative measurements, the two methods agree. When changing the potentials, however, the second method can sometimes fail to work altogether. Hence although computationally simpler, in general the first method is probably better in most cases.

C Transition finding algorithms

C.1 Chiral transition

Recall that the chiral transition is given by the boundary ∂V of the area A in the $(\lambda_h, \tilde{B})$-plane where a chirally broken solution exists. One might note that we really need to look at the boundary ∂W of the area W in the (T, B)-plane where such a solution exists, because in principle it could be that there exists a line in the interior of V which maps to the boundary of W. In fact, it turns out that for our system, there is indeed such a line. However, it also turns out that that line is not in the dominant phase because it is dominated by confined

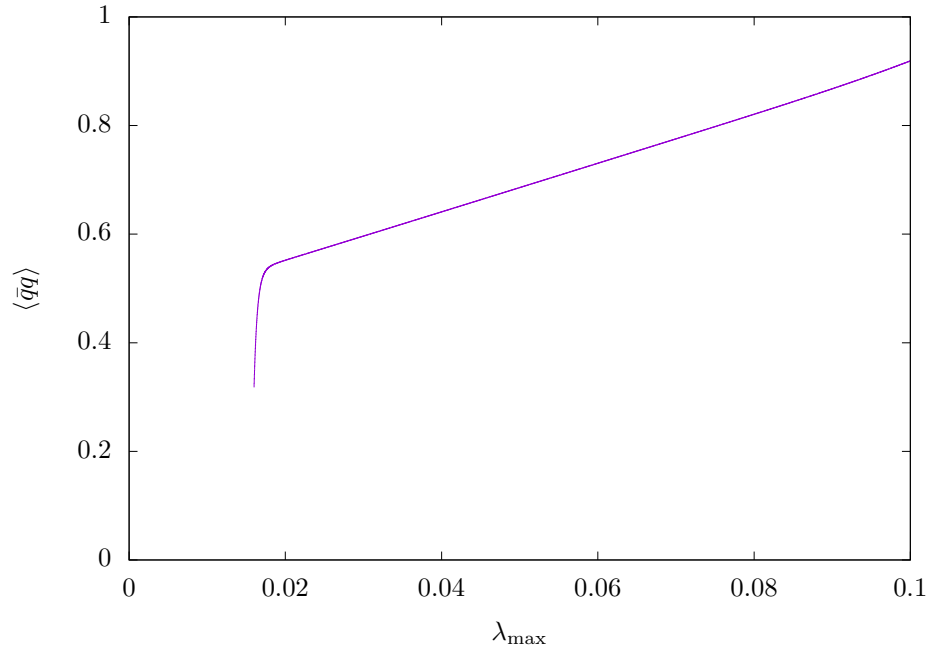

Figure 18: $\langle \bar{q}q \rangle$ as a function of $A_{\max}$, plotted against $\lambda_{\max}$. As can be seen here, the graph is linear for a while, and then it deviates.

solutions. This means that indeed we need to find ∂V. Note that once ∂V is found, ∂W can easily be found by the means described in the previous section.

This was done in two steps. First, the $(\lambda_h, \tilde{B})$-plane was explored using a grid to get a general idea of the shape of the area V. This is necessary because the next step requires a parameterization (x, y) of the $(\lambda_h, \tilde{B})$-plane such that for each x there is precisely one y which lies on ∂V. In the course of this thesis, as different potentials were tried, three different parameterizations were used, namely

- Cartesian coordinates $x = \tilde{B}$ and $y = \lambda_h$,
- Polar coordinates around $\lambda_h = 1$, $\tilde{B} = 0$, with $x = r$ and $y = \theta$,
- 'Scaled' polar coordinates, in which the radius is given by $r^2 = 9\lambda_h^2 + \tilde{B}^2$, again with $x = r$ and $y = \theta$.

For the potentials given in the final version of this thesis, the second option was used.

The second step is simple, but to obtain a solution within a reasonable time frame requires some work. Since ∂V is defined by existence of a chirally broken solution, it can, for each x, be found by using a binary search in y. The interesting question is with what bounds to start the search. Too large a bound will make the computation take a long time, while too small a bound might cause no solution to be found since the solution doesn't lie within the bound. The solution used in this thesis is to first compute a starting point for $x = 0$

with a known bound, and then use the following algorithm for other x, which are chosen in a regular grid:

1. Locate the closest known point on ∂W.[15] The bound is then estimated to be centered around the same y as the closest known point. This is another reason why it is important to choose a reasonable parameterization. For a reasonable parameterization, this guess will often be close to the point we're looking for. The size of the bound is then estimated as a linear function of the distance in units of x to the point used to make the estimate.

2. Check that for the lowest y in the bound there is no chirally broken solution, and that for the highest y in the bound there is a chirally broken solution. If this is true, we know that the point we're looking for lies somewhere in the middle, so we proceed to step 3. If not, then by the construction of the parameterizations, we can deduce from existence on either side of the bound whether we should increase or decrease y. If for both ends there is no chirally broken solution, then we move the new bottom of the bound to the top of the old one, and we double the size, so that if we're really far away from the correct solution, it will take less time.[16] Likewise, if both ends exist, we move the new top of the bound to the bottom of the old one, and also double the size. Note that in each parameterization we must take care not to end up in situations where $\lambda_h \leq 0$. This step is repeated until we have existence at the top of the bound and non-existence at the bottom.

3. Do a binary search within the bound to find the desired point to within the desired accuracy.

C.2 Deconfinement transition

The deconfinement transition is a bit more difficult to compute. As was mentioned in the main body of the text, the confining transition occurs where the free energy of a solution is the same as that of a thermal gas solution with the same magnetic field. It was also mentioned that thermal gas solutions can be taken to be solutions with a small black hole, i.e. $A_h \ll 1$. It also turns out that this corresponds to solutions with $\lambda_h \gg 1$. Lastly, we can use the relation $\mathrm{d}F = -S\,\mathrm{d}T$ for fixed B. Putting this together, we can conclude that

$$F = -\int_\gamma S(\gamma(t))\frac{\partial T(\gamma(t))}{\partial t}\,\mathrm{d}t,$$

where and $\gamma(t)$ is a path along which B is constant, where the end of the path corresponds to the point we want to know the free energy of, and the start of the path corresponds to the point of large λ_h. Note that this integral is well-approximated if we truncate it at some large λ_h, since those solutions have a small black hole, and so S becomes small in that limit. In this thesis doubling

[15] This is not always the adjacent point in the grid, since the algorithm is multi-threaded to take advantage of the parallel nature of modern CPUs.

[16] This obviously takes more time in other solutions, but from testing this turned out to be fastest.

or halving the truncation point revealed no discernible change in F, indicating that the integration is accurate. The remaining question is how such a path can be found, and the answer used in this thesis is to determine the derivative $DB(\lambda_h, \tilde{B})$ by looking at nearby points, and using it to find the direction along which B is constant and λ_h increases.[17] Note that by doing this integration, one calculates the free energies of every point on the integration path, so we can also easily determine where it is zero, yielding the deconfinement transition. In practice, for these potentials, we start the integration from the chiral transition. This has as an advantage that it handles the following exception well, which occurs for large B, and may be physical or just due to numerical error. For large enough B the above method will yield no zeros, and the chiral transition line will turn out to have a positive free energy compared to the point with large λ_h. This means that the chiral transition in this case is not in the dominant phase, but from it, we can integrate further from the chiral transition into the direction in which λ_h decreases, namely in the chirally symmetric phase. This we can do because it turns out that the values for τ_h near the chiral transition approach zero, which means that the solutions continuously approach the chirally symmetric ones. After continuing the integration we then find the deconfinement transition, where now the deconfinement transition doesn't separate the confined phase from the chirally broken phase, but the confined phase from the chirally symmetric phase.

References

[1] B. Abelev et al. Charge separation relative to the reaction plane in pb-pb collisions at $\sqrt{s_{NN}}$=2.76 TeV. *Phys. Rev. Lett.*, 110:012301, Jan 2013.

[2] T. Alho, M. Järvinen, K. Kajantie, E. Kiritsis, C. Rosen, and K. Tuominen. A holographic model for QCD in the Veneziano limit at finite temperature and density. *JHEP*, 04:124, 2014. [Erratum: JHEP02,033(2015)].

[3] T. Alho, M. Järvinen, K. Kajantie, E. Kiritsis, and K. Tuominen. On finite-temperature holographic QCD in the Veneziano limit. *JHEP*, 01:093, 2013.

[4] Daniel Areán, Ioannis Iatrakis, Matti Järvinen, and Elias Kiritsis. The discontinuities of conformal transitions and mass spectra of V-QCD. *JHEP*, 11:068, 2013.

[5] G. S. Bali, F. Bruckmann, G. Endrodi, Z. Fodor, S. D. Katz, S. Krieg, A. Schafer, and K. K. Szabo. The finite temperature QCD transition in external magnetic fields. *PoS*, LATTICE2011:192, 2011.

[6] G. S. Bali, F. Bruckmann, G. Endrodi, Z. Fodor, S. D. Katz, S. Krieg, A. Schafer, and K. K. Szabo. The QCD phase diagram for external magnetic fields. *JHEP*, 02:044, 2012.

[17] Note that for some potentials this path might not have λ_h increasing everywhere along such a path. In this case alternatively one can integrate in the direction in which B is constant and S decreases.

[7] G. S. Bali, F. Bruckmann, G. Endrodi, Z. Fodor, S. D. Katz, and A. Schafer. QCD quark condensate in external magnetic fields. *Phys. Rev.*, D86:071502, 2012.

[8] Jacob D. Bekenstein. Black holes and entropy. *Phys. Rev. D*, 7:2333–2346, Apr 1973.

[9] V. V. Braguta, P. V. Buividovich, T. Kalaydzhyan, S. V. Kuznetsov, and M. I. Polikarpov. The Chiral Magnetic Effect and chiral symmetry breaking in SU(3) quenched lattice gauge theory. *Phys. Atom. Nucl.*, 75:488–492, 2012.

[10] Falk Bruckmann, Gergely Endrodi, and Tamas G. Kovacs. Inverse magnetic catalysis and the Polyakov loop. *JHEP*, 04:112, 2013.

[11] Falk Bruckmann, Gergely Endrodi, and Tamas G. Kovacs. Inverse magnetic catalysis in QCD. 2013.

[12] P. V. Buividovich, M. N. Chernodub, E. V. Luschevskaya, and M. I. Polikarpov. Lattice QCD in strong magnetic fields. *eCONF*, C0906083:25, 2009.

[13] P. V. Buividovich, M. N. Chernodub, E. V. Luschevskaya, and M. I. Polikarpov. Numerical study of chiral symmetry breaking in non-Abelian gauge theory with background magnetic field. *Phys. Lett.*, B682:484–489, 2010.

[14] Jorge Casalderrey-Solana, Hong Liu, David Mateos, Krishna Rajagopal, and Urs Achim Wiedemann. Gauge/String Duality, Hot QCD and Heavy Ion Collisions. 2011.

[15] Massimo D'Elia. Lattice qcd in background fields. *Journal of Physics: Conference Series*, 432(1):012004, 2013.

[16] Massimo D'Elia. Lattice QCD Simulations in External Background Fields. *Lect. Notes Phys.*, 871:181–208, 2013.

[17] Massimo D'Elia, Swagato Mukherjee, and Francesco Sanfilippo. QCD Phase Transition in a Strong Magnetic Background. *Phys. Rev.*, D82:051501, 2010.

[18] Massimo D'Elia and Francesco Negro. Chiral Properties of Strong Interactions in a Magnetic Background. *Phys. Rev.*, D83:114028, 2011.

[19] J.R. Dormand and P.J. Prince. A family of embedded Runge-Kutta formulae. *Journal of Computational and Applied Mathematics*, 6(1):19 – 26, 1980.

[20] Nick Evans, Carlisson Miller, and Marc Scott. Inverse Magnetic Catalysis in Bottom-Up Holographic QCD. 2016.

[21] S. S. Gubser, Igor R. Klebanov, and Alexander M. Polyakov. Gauge theory correlators from noncritical string theory. *Phys. Lett.*, B428:105–114, 1998.

[22] U. Gürsoy and E. Kiritsis. Exploring improved holographic theories for QCD: Part I. *JHEP*, 02:032, 2008.

[23] U. Gürsoy, E. Kiritsis, L. Mazzanti, and F. Nitti. Holography and Thermodynamics of 5D Dilaton-gravity. *JHEP*, 05:033, 2009.

[24] U. Gürsoy, E. Kiritsis, L. Mazzanti, and F. Nitti. Improved Holographic Yang-Mills at Finite Temperature: Comparison with Data. *Nucl. Phys.*, B820:148–177, 2009.

[25] U. Gürsoy, E. Kiritsis, and F. Nitti. Exploring improved holographic theories for QCD: Part II. *JHEP*, 02:019, 2008.

[26] Umut Gürsoy, Elias Kiritsis, Liuba Mazzanti, Georgios Michalogiorgakis, and Francesco Nitti. Improved Holographic QCD. *Lect. Notes Phys.*, 828:79–146, 2011.

[27] Tetsuo Hatsuda and Teiji Kunihiro. QCD phenomenology based on a chiral effective Lagrangian. *Phys. Rept.*, 247:221–367, 1994.

[28] S. W. Hawking. Particle creation by black holes. *Communications in Mathematical Physics*, 43(3):199–220, 1975.

[29] E. M. Ilgenfritz, M. Kalinowski, M. Muller-Preussker, B. Petersson, and A. Schreiber. Two-color QCD with staggered fermions at finite temperature under the influence of a magnetic field. *Phys. Rev.*, D85:114504, 2012.

[30] E. M. Ilgenfritz, M. Muller-Preussker, B. Petersson, and A. Schreiber. Magnetic catalysis (and inverse catalysis) at finite temperature in two-color lattice QCD. *Phys. Rev.*, D89(5):054512, 2014.

[31] Matti Järvinen and Elias Kiritsis. Holographic Models for QCD in the Veneziano Limit. *JHEP*, 03:002, 2012.

[32] Dmitri E. Kharzeev. The Chiral Magnetic Effect and Anomaly-Induced Transport. *Prog. Part. Nucl. Phys.*, 75:133–151, 2014.

[33] Qiang Li, Dmitri E. Kharzeev, Cheng Zhang, Yuan Huang, I. Pletikosic, A. V. Fedorov, R. D. Zhong, J. A. Schneeloch, G. D. Gu, and T. Valla. Observation of the chiral magnetic effect in ZrTe5. *Nature Phys.*, 12:550–554, 2016.

[34] Juan Martin Maldacena. The Large N limit of superconformal field theories and supergravity. *Int. J. Theor. Phys.*, 38:1113–1133, 1999. [Adv. Theor. Math. Phys.2,231(1998)].

[35] Vladimir A. Miransky and Igor A. Shovkovy. Quantum field theory in a magnetic field: From quantum chromodynamics to graphene and Dirac semimetals. *Phys. Rept.*, 576:1–209, 2015.

[36] Marco Panero. Thermodynamics of the QCD plasma and the large-N limit. *Phys. Rev. Lett.*, 103:232001, 2009.

[37] Leonard Susskind. The World as a hologram. *J. Math. Phys.*, 36:6377–6396, 1995.

[38] Gerard 't Hooft. A Planar Diagram Theory for Strong Interactions. *Nucl. Phys.*, B72:461, 1974.

[39] Gerard 't Hooft. Dimensional reduction in quantum gravity. In *Salamfest 1993:0284-296*, pages 0284–296, 1993.

[40] Edward Witten. Anti-de Sitter space and holography. *Adv. Theor. Math. Phys.*, 2:253–291, 1998.